Andreas Hofer, BSc

Physical Vapor Deposition and Characterisation of Decyl-Phenyl-Benzothieno-Benzothiophene Thin Films

MASTER'S THESIS

to achieve the university degree of

Diplom-Ingenieur

Master's degree programme: Advanced Materials Science

submitted to

Graz University of Technology

Supervisor

Ao.Univ.-Prof. Dipl.-Ing. Dr.techn. Roland Resel

Institute of Solid State Physics

Graz, May 2019

AFFIDAVIT

I declare that I have authored this thesis independently, that I have not used other than the declared sources/resources, and that I have explicitly indicated all material which has been quoted either literally or by content from the sources used. The text document uploaded to TUGRAZonline is identical to the present master‘s thesis.

Date

Signature

Acknowledgement

First and foremost, I would like to thank my supervisor Roland Resel for the topic of this thesis, his support as well as his supervision. Secondly, Mike Ramsey and the Surface Science group of the Institute of Physics of the University of Graz for their cooperation and support with the preparation of the samples. In addition, my colleagues at Graz University of Technology, in particular Wolfgang Bodlos, Sebastian Hofer, Johanna Unterkofler, Benedikt Schrode, Jacopo Remondina and Clemens Tschernay as well as the entire Institute of Solid State Physics of Graz University of Technology. Furthermore, I would like to thank Luca Beverina of the University of Milano-Bicocca for supplying the molecule used in this thesis. Last but not least I would like to thank my family and friends for their continued support throughout the years.

Abstract

Benzothieno[3,2-b][1] benzothiophene-derivatives gained interest in the scientific community due to their organic semiconducting properties, specifically a high charge carrier mobility in organic thin film transistors. In addition, it has been demonstrated that the derivative used in this thesis, 2-decyl-7-phenyl-[1] benzothieno[3,2-b][1] benzothiophene (Ph-BTBT-10), transitions into liquid crystalline phases. Furthermore, molecularly flat films can be produced by spin coating at elevated temperatures with the addition of a subsequent thermal treatment. In this work, films of varying thicknesses ranging from nominal submonolayers (20 Å) to multilayers (600 Å) were prepared by physical vapor deposition on silicon wafers. Films were investigated in terms of layer morphology and film properties by atomic force microscopy and X-ray reflectometry as well as crystalline properties by specular X-ray diffraction and grazing incidence X-ray diffraction. The measurements show that samples with a nominal thickness of 81 Å and less can be described by a repeating unit containing two upright standing molecules on top of each other as described by the bulk structure. In addition, it is shown, that samples with a nominal thickness of 20 – 30 Å form double-layer islands with a height of 55 Å. With increasing nominal film thickness. This structure grows in coverage and crystallites form in between the double-layers. Starting from a nominal thickness of 107 Å another type of molecular packing appears which arises from an unknown polymorph. This new structure differs from the known packing motif mainly through the length of the long unit cell axis. In addition, the peak positions of the new structure are slightly shifted relative to the positions of the known bulk phase. Additionally, a change in morphology can be observed in samples with a thickness of more than 107 Å. Furthermore, it is shown, that the new crystal structure is a metastable phase, that transitions to the bulk structure at a temperature of 110°C.

Kurzfassung

Benzothieno[3,2-b][1] benzothiophen-derivate sind für der Wissenschaft aufgrund ihrer halbleitenden Eigenschaften, besonders ihre hohe Ladungsträgermobilität in organischen Dünnschicht Transistoren, interessant. Zusätzlich wurden für das in dieser Arbeit verwendete Molekül, 2-decyl-7-phenyl-[1] benzothieno[3,2-b][1] benzothiophen (Ph-BTBT-10) Phasenübergänge zu Flüssigkristallphasen entdeckt. Außerdem wurden bereits molekular flache Ph-BTBT-10 Filme durch Rotationsbeschichten bei erhöhten Temperaturen und eine anschließende Temperaturbehandlung hergestellt. In dieser Arbeit wurden Filme mit Schichtdicken von 20 Å bis mehr als 600 Å durch physikalische Gasphasenabscheidung auf Silizium Wafern hergestellt. Die Filme wurden dann auf ihre Morphologie und Filmeigenschaften mithilfe von Rasterkraftmikroskopie und Röntgenreflektometrie und ihre Kristallstruktur durch spekulare Röntgendiffraktometrie und Röntgenbeugung mit streifendem Einfall untersucht. Die Messungen zeigen, dass Proben mit einer nominellen Schichtdicke von weniger als 81 Å durch eine Wiederholeinheit von zwei aufrecht aufeinanderstehenden Molekülen beschrieben werden können. Zusätzlich wird gezeigt, dass Proben mit einer nominellen Schichtdicke von 20 – 30 Å Doppellageninseln mit einer Höhe von 55 Å bilden. Der Bedeckungsgrad dieser Struktur steigt mit einem Anstieg der Filmdicke und Kristallite werden zwischen dem Film gebildet. Ab einer Schichtdicke von 107 Å kann eine neue polymorphe Phase gesehen werden. Diese Struktur unterscheidet sich von der bekannten Kristallstruktur hauptsächlich durch ein Halbieren der Länge der längsten Einheitszellenachse. Zusätzlich kann ein leichtes Schieben der gemessenen Peaks im Vergleich zu den Positionen der bekannten Struktur beobachtet werden. Außerdem kann eine Veränderung der Morphologie, durch das Auftreten von länglichen Inseln, in Proben mit einer Schichtdicke von mehr als 107 Å bestimmt werden. Abschließend wurde noch gezeigt, dass es sich bei der neuen Phase um eine metastabile Phase, die bei einer Temperatur von 110°C in die bekannte Struktur übergeht, handelt.

Table of Contents

Fundamentals

Polymorphism and Substrate Induced Phases

Polymorphism describes the effect, that more than one crystal structure exists for a given material. It is especially important when considering and characterising polymorphic phases for organic semiconductors because charge transport as well as the electronic band structure depend on the crystal structure, due to a change in overlap of π-orbitals with a change of the packing motif [1].

Thin film- or substrate induced phases appear due to interaction between the film with the substrate and need to be distinguished from polymorphs that appear due to bulk crystallisation from a supersaturated solution or vapour growth and are also present in films with high film thickness.

The characterisation of thin film phases, which have been shown to be present in multiple organic semiconductors [2]–[4], is of utmost importance for charge transport, because transport takes place close to the substrate/organic interface. Thin film phases exist in films up to a critical thickness at which a bulk crystal phase appears. Above this film thickness a structure-change is observed. For example in case of pentacene it has been shown that the thin film phase can convert to a bulk phase [5]. The bulk phase and the substrate induced phase have been shown to also coexist in case of dioctyl-terthiophene, which leads to the bulk phase growing

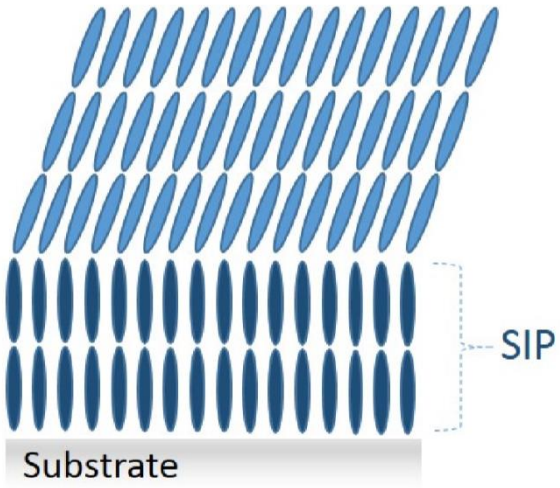

Fig. 1: Schematic illustration of a bulk crystal phase growing on top of a surface induced phase [18]

on top of the surface induced phase [6], [7]. It is not fully understood what causes the appearance of thin film phases. While it has been shown, that the surface induced phase of pentacene is actually not dependent on a substrate surface, but instead on the presence of a monolayer of upright standing pentacene-molecules beneath [8], the formation of a wetting layer of 2,7-dioctyl-BTBT at the substrate/organic interface is very sensitive to the nature of the substrate [6].

For polymorphs that appear in thicker films, away from the substrate surface an influence of the deposition method as well as the conditions needs to be considered. For spin coated samples interactions between the molecule and the solvent as well as the evaporation rate of the solvent and the spin speed of the sample can impact the crystal structure of the film. In case of samples prepared by physical vapour deposition, a change in evaporation rate can yield a different polymorph. This can be explained, by the fact, that a fast solvent evaporation during spin coating as well as a high evaporation rate during physical vapour deposition describe systems far from their equilibrium state, which can lead to kinetic trapping of metastable states [4], [9].

Furthermore it needs to be considered that these phases are not the energetically most favourable form and slowly transform into the bulk phase over time or by annealing, which further indicates that they are indeed metastable [2].

Decyl-Phenyl-Benzothieno-Benzothiophene

In organic semiconductor research, two groups of materials gained major attention. The more established one being π-conjugated polymers and the other one being small molecules. Although polymers are the more common material, there are some drawbacks that restrict device performance and ease-of-processing. Polymers often run into the issue of charge carrier trapping due to a statistical distribution of the molecular size as well as mislinkage of monomers. In comparison molecular semiconductors form well-ordered structures and have easier-to-control properties. Additionally, polymers also lack in solution-process ability due to their size. In contrast to that, smaller molecules are already easier to process and their dissolubility can be further improved through the addition of functional groups [10], [11].

Among molecular semiconductors, benzothieno-benzothiophene-derivatives gained interest as promising candidates in organic electronics applications due to several molecules in this group exhibiting a high charge carrier mobility in organic thin film transistors (OTFT) [10]–[12]. When looking at the electronic properties, it is important to note that BTBT-derivatives have been shown to form polymorphic

phases [2], [13]. For possible applications it also needs to be mentioned, that the issue of oxidation of the material at air doesn't arise [10].

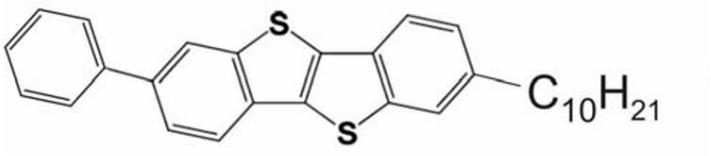

Fig. 2: Chemical structure of Ph-BTBT-10 with a phenylgroup on one side, the benzothienobenzothiophene unit in the center and the decylgroup to the other side

Out of the BTBT derivatives, Ph-BTBT-10 is of special interest, because it is an asymmetric molecule. In addition, the molecule exhibits a particularly high charge carrier mobility in organic thin film transistors, that can be further enhanced by a thermal treatment at 120°C. Important to note is, that this temperature is slightly below a phase transition temperature to a *crystal E* phase. Generally, the material exhibits a transition from a crystalline into a *crystal E* phase at 143°C as well as a *smectic A* phase above 210°C, that is stable up to 223°C when the material melts [12].

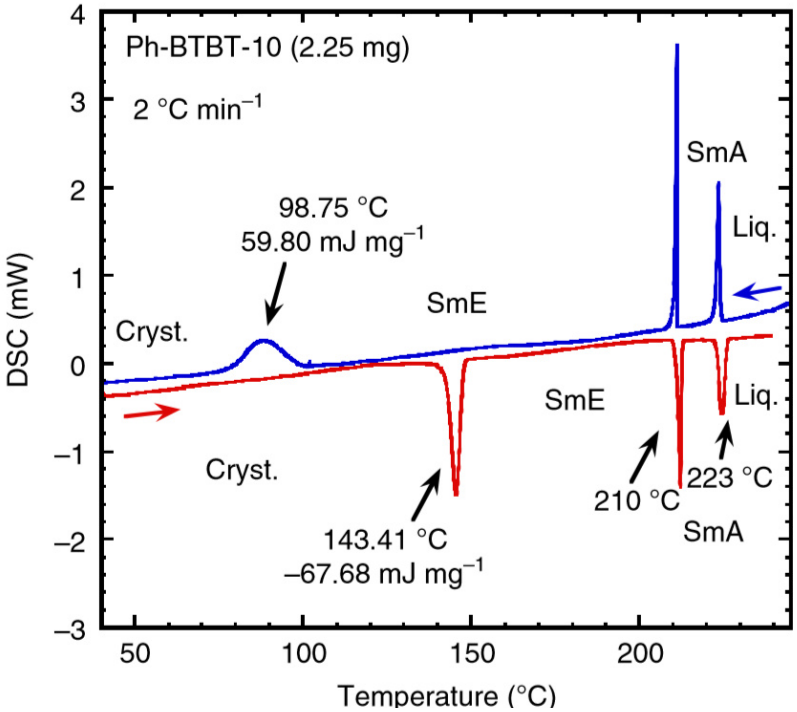

Fig. 3: Differential scanning calorimetry measurement showing the phase transition behavior of the molecule [12]

A crystal structure of Ph-BTBT-10 has already been determined for single crystals. In the known structure, the molecules pack in a head-to-head arrangement along the long unit cell axis with a herringbone arrangement in the ab-plane as can be seen in Fig.4 [14].

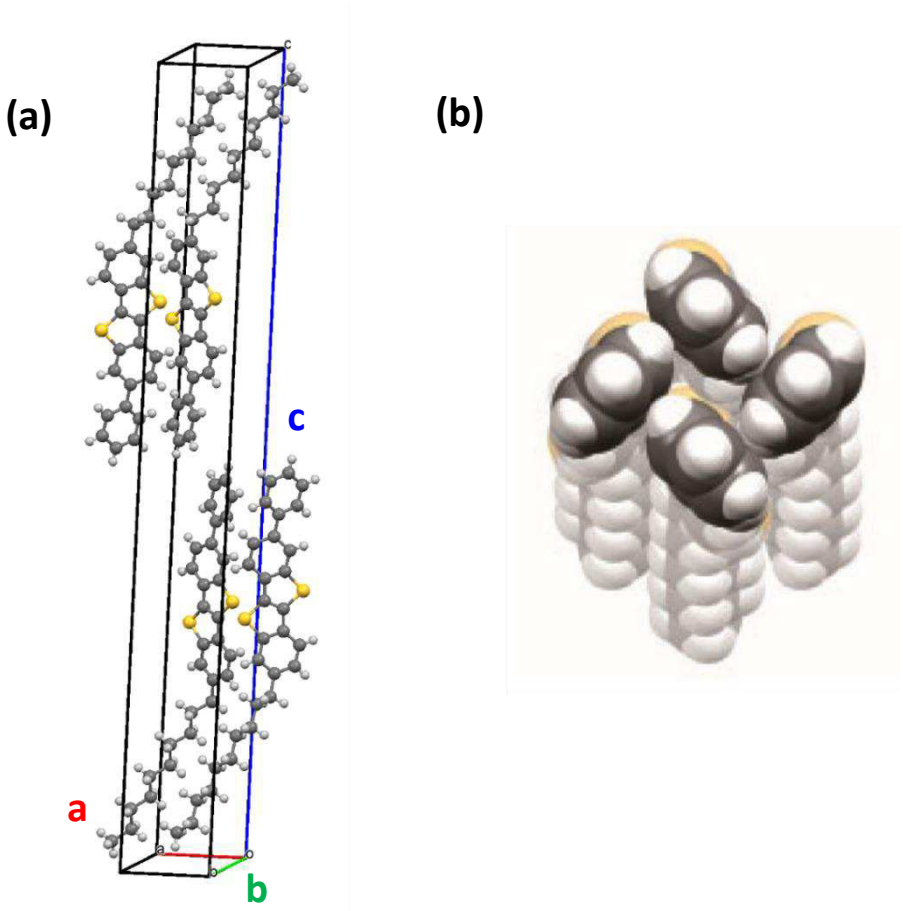

Fig. 4: Unit cell of the bulk-structure with head-to-head arrangement (a) and herringbone packing motif in the ab-plane of Ph-BTBT-10 (b) [14]

Experimental Techniques

Physical Vapor Deposition

Physical Vapor Deposition (PVD) describes deposition methods in which a material enters the gas phase by physical means (i.e. through evaporation or collision) and arrives at a substrate without a chemical interaction occurring. The method used in this thesis is thermal evaporation in ultra-high vacuum (UHV). Therefore, the material was put in a Knudsen cell in powder-form and evaporated at temperatures of 260 – 280 °C. The cell consisted of a ceramic crucible with a tungsten wire threaded through acting as a heating filament. Furthermore, an Aluminium cap with a thermocouple underneath was used as an aperture and the whole device was water-cooled to stabilise the temperature.

The pressure in the chamber before and after evaporation was approximately 10^{-9} mbar and around 10^{-8} mbar during evaporation. To maintain a good base pressure, the samples were transported out of the chamber through a transfer chamber that was flushed with Argon when going to ambient pressure to minimize the amount of water in the chamber.

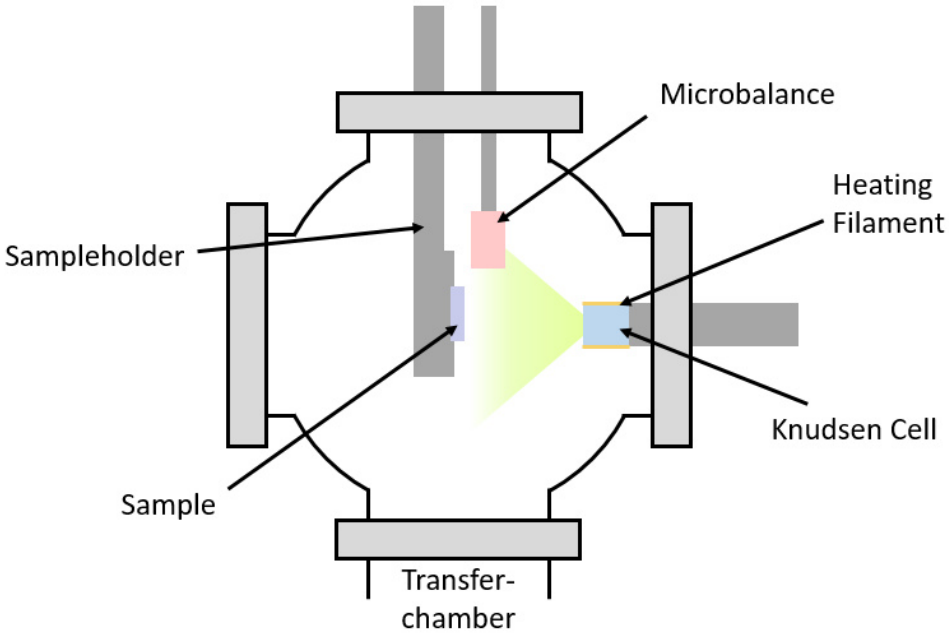

Fig. 5:Schematic overview of the preparation-chamber used in this thesis

The evaporation rate was measured before and after sample preparation with a quartz microbalance, because it was impossible to measure during the thin film preparation process. This was necessary because the microbalance needed to be in the same spot during measurement as the sample during preparation to ensure a reliable rate. Before the preparation a stable rate of approximately 10 Å/min was adjusted.

Samples

For this entire thesis 10 x 10 mm² silicon wafers with a 150 nm thermal oxide layer were used. The substrates are coated with a 2 nm organic protection layer which needed to be removed before preparation. This was performed by placing them in acetone and cleaning with an ultrasonic bath for 5 min. This procedure was repeated with ethanol. Afterwards the wafers were rinsed with acetone and ethanol and dried with air. To ensure that the substrates were properly cleaned exemplary X-ray reflectivity measurements on empty wafers were performed as can be seen in Fig. 6. Kiessig fringes that correspond to a layer thickness of approximately 2 nm can't be observed, while small fringes matching the 150 nm oxide layer are present in the measurement of a cleaned substrate. In comparison the X-ray reflectivity measurement of an uncleaned wafer clearly shows a Kiessig fringe that correlates with a film thickness of approximately 2 nm.

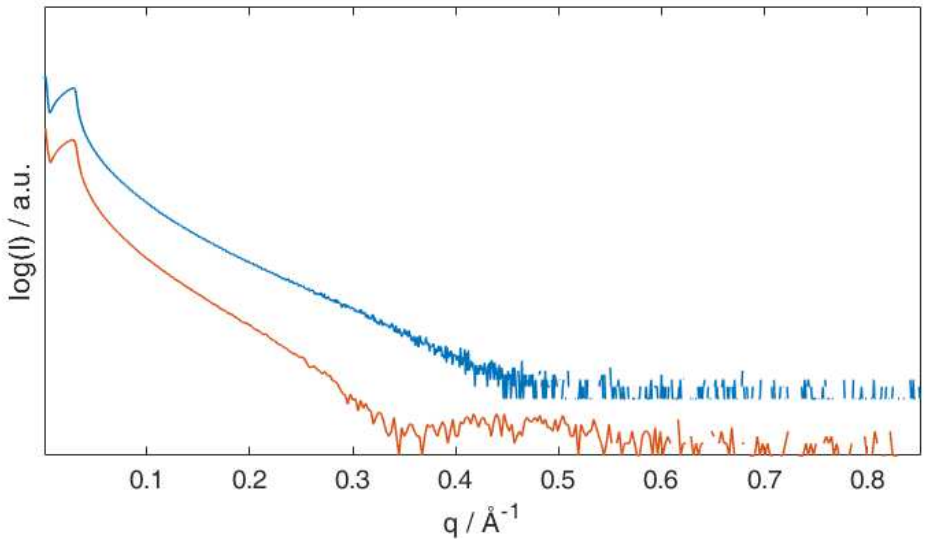

Fig. 6: X-ray reflectivity curve of a cleaned substrate (blue) as well as a substrate with the organic protection layer still on (orange)

Subsequently samples of varying Ph-BTBT-10-layer thickness were prepared as is shown in Tab. 1. It is important to note, that for the first series the nominal thickness, determined through the microbalance increasingly deviates from the thickness measured by X-ray reflectivity with increasing layer thickness. The second

series was performed to correct the error in film thickness observed in the first series and validate a change in crystal structure observed in the first series. In addition, the goal of the third series was the determination of a critical thickness for the structure change observed in the first two series. All series were performed with comparable deposition rates as well as a similar pressure in the preparation chamber to ensure reproducibility. Further the low deposition rate for the 151 Å sample in the third series as well as the layer thickness in the 778 Å sample of the second series are caused by the fact that the evaporator ran out of material during deposition.

Table 1: Sample overview with layer thickness and evaporation conditions
d_{nom} … Nominal layer thickness determined through the rate and deposition time
d_{XRR} … Nominal layer thickness determined by XRR, corrected for reduced coverage through AFM measurements
t … Deposition time
n_i … Average evaporation rate during deposition
p … Average pressure in the chamber during deposition

series	d_{nom} / Å	d_{XRR} / Å	t / min	n_i / Å/min	p / 10^{-8} mbar
1st series	15	13	1,75	8,75	1,6
	29	22	3	9,50	1,4
	50	33	6	8,25	1,2
	108	48	12	9,00	0,8
	345	87	30	11,50	0,9
	725	157	50	14,50	1,5
	1169	179	85	13,75	1,4
2nd series	30	25	2,3	12,90	3,7
	54	60	6	9,00	4,6
	127	109	11	11,50	5,1
	282	220	24	11,75	2,6
	582	484	60	9,70	4,5
	778	737	80	9,73	2,8
3rd series	47	46	4,5	10,40	1,9
	49	54	5	9,75	1,8
	70	69	7	9,95	2,7
	84	81	9	9,38	2,3
	112	107	13,3	8,40	1,5
	140	129	15,3	9,15	1,9
	151	141	25	6,03	1,7
	203	177	20	10,13	1,8

Atomic Force Microscopy

Atomic force microscopy (AFM) is a scanning probe microscopy technique, that measures features on a surface by scanning the surface with a tip on a cantilever through interactions between the surface and the tip. The deflection and oscillation of this cantilever are monitored through an optical system, consisting of a laser, that gets reflected by the cantilever and a photodetector that measures the displacement or oscillation amplitude of the cantilever. Through a feedback loop the oscillation amplitude or deflection is then adjusted via piezo tubes.

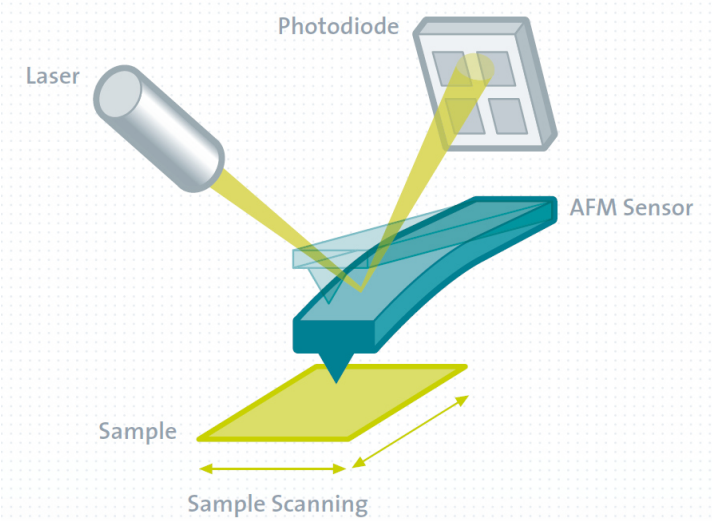

Fig. 7: Schematic illustration of an AFM setup with tip, cantilever and optical detection system [19]

Generally, it is important to differentiate between three measurement modes, the first one being the contact mode. Here the AFM-tip and the sample are in constant contact and repulsive forces act on the tip due to Pauli-repulsion. The biggest disadvantage of this mode is that the tip gets drawn across the sample-surface which can deform, scratch or delaminate soft samples. Another measurement mode is the non-contact mode, which is defined by the fact that during the measurement the sample and the AFM-tip are never in contact. The measurement principle of this mode is that the tip is oscillated above the surface with a constant frequency, while changes in the oscillation amplitude, which are usually caused by van der Waals forces between tip and sample, are measured. The most common mode is a combination of those two. In tapping mode, the tip is oscillated with a constant frequency above the sample and again the amplitude is measured. It differs from the aforementioned modes by the occurrence of repulsive as well as attractive forces between tip and sample, because the tip comes in contact with

the sample for a short time during oscillation. This has the advantages of reduced sample damage compared to contact mode as well as improved resolution in comparison with non-contact mode.

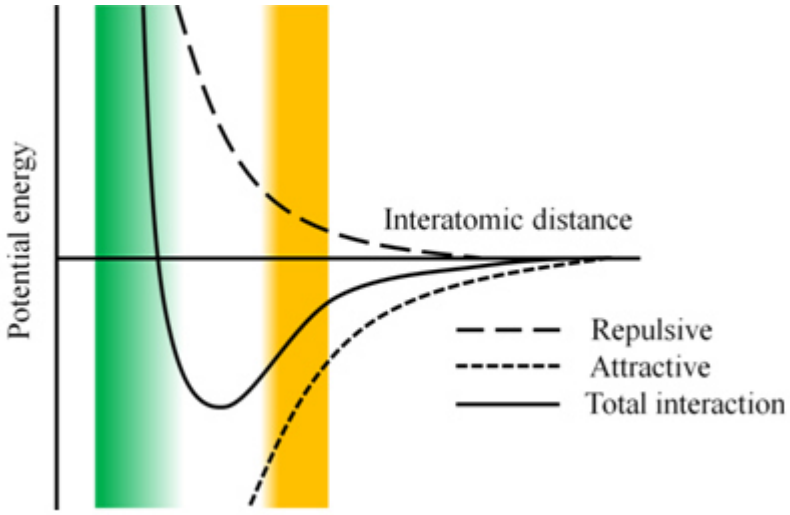

Fig. 8: Potential with the regime of the contact mode indicated in green and the regime for non-contact mode in orange [20]

AFM measurements give insight on the surface morphology through a height image, where shape and size of features on the surface can be determined. In addition, through the phase shift of the oscillation frequency further information on a change in material, properties or morphology can be gained. Together with the height information, a change in material can therefore be determined and differentiated from a change in morphology.

X-Ray Reflectivity

X-Ray reflectivity (XRR) is a thin film characterisation method, that is mainly used to determine film thickness, but can also be used for the evaluation of surface or interface roughness or film density. The measurement principles for XRR are reflection and transmission of X-rays for incidence angles above the critical angle of total reflection. This is further described by the refractive index in (2.1),

$$n = 1 - \delta + i\beta \tag{2.1}$$

with δ describing the refractive index decrement

$$\delta = \frac{\lambda^2}{2\pi} * r_e * \rho_e \tag{2.2}$$

and β being the absorption term.

$$\beta = \frac{\lambda}{4\pi} * \mu_x \tag{2.3}$$

Here r_e describes the classical electron radius, ρ_e the electron density in the solid and μ_x the linear absorption coefficient. With (2.1) and Snell's law

$$n_1 * cos\alpha_1 = n_2 * cos\alpha' \tag{2.4}$$

under consideration that $n_1 = 1$ for air, $\beta \approx 0$ since absorption is negligible and $\alpha' = 0$ the critical angle of total reflection is:

$$\alpha_c = \sqrt{2\delta} \tag{2.5}$$

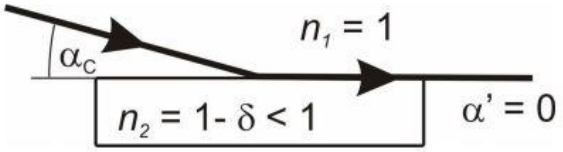

Fig. 9: Beam path for total external reflection [21]

Below this angle X-rays can't transmit into the sample, so the only information that can be obtained from the critical angle is the electron density of the sample. At higher incidence angles X-rays can transmit into the sample. This leads to a

transmitted as well as a reflected beam at every interface in the sample. The reflected beams can then interfere with each other, which leads to the characteristic Kiessig fringes, that correlate with the film thickness. Furthermore, the roughness of the film and the substrate can be determined through reduced reflected intensity due to diffuse scattering at the surface or the film/substrate interface.

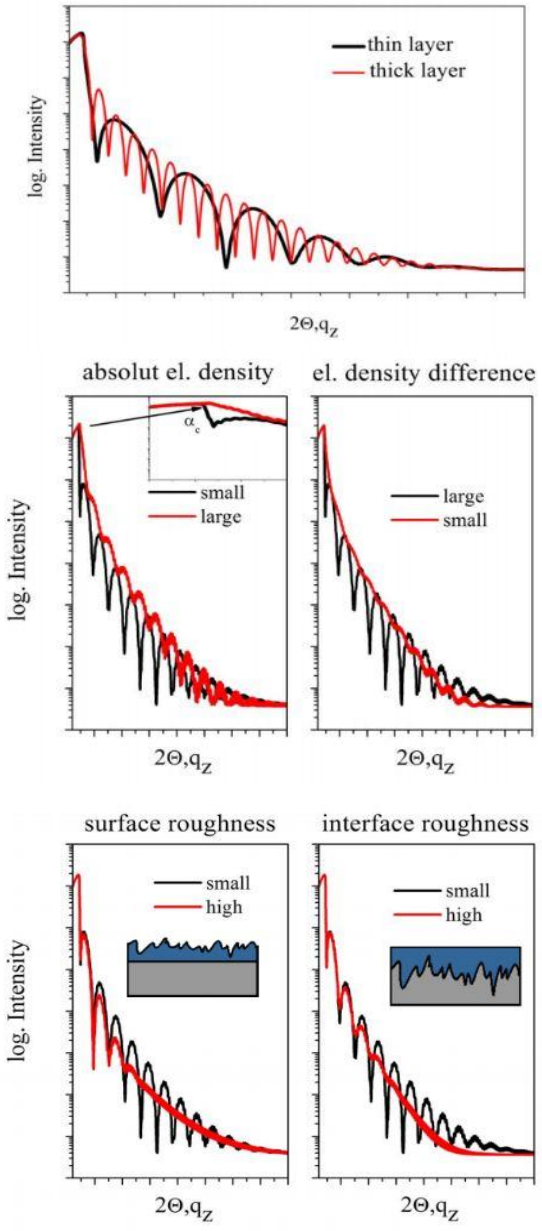

Fig. 10: Influence of the layer thickness, electron density and interface as well as surface roughness on the XRR signal [22]

All samples in this thesis were measured with a Panalytical Empyrean with Cu-K_α radiation (λ = 0.154 nm) and incidence angles between 0° and 6° under specular condition. On the primary side a 1/32° divergence slit and a 4 mm mask were mounted. The side of the X-ray tube also contains a parallel beam mirror as well as a 0.125 mm Ni-plate as a beam attenuator to protect the detector in case of the intensity rising above a certain count rate. On the detector side, a 0.1 mm anti-scatter slit and a 0.02 Soller slit were mounted between the sample and the point detector.

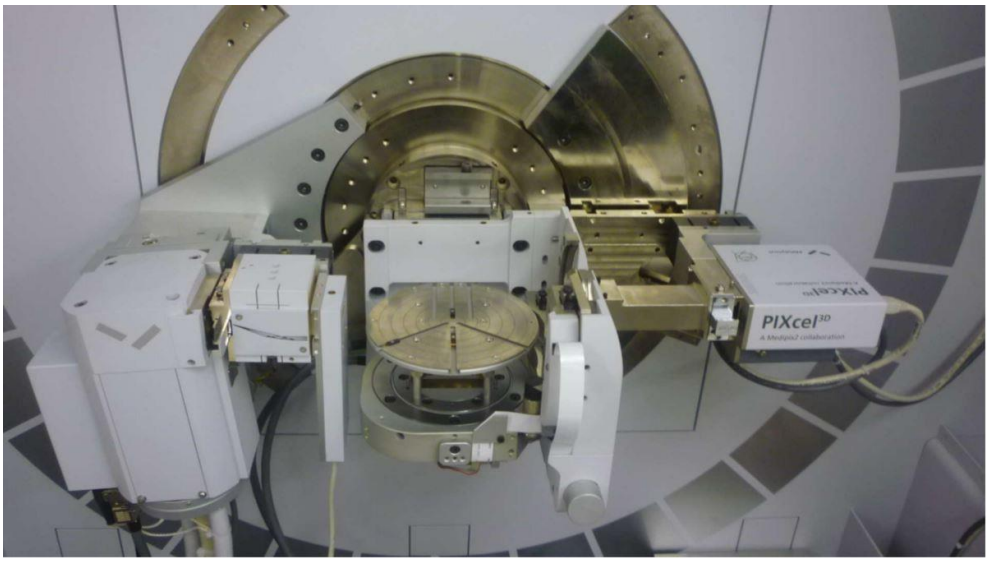

Fig. 11: Setup of the Panalytical Empyrean with the incoming beam to the left and the outgoing beam to the right [13]

Data Evaluation

For the determination of film parameters, a fit of the reflectivity curve needs to be performed. This data evaluation was accomplished by a model dependent fit with the Panalytical X'Pert Reflectivity software as well as a model independent fit with the software Stochfit. Both software packages are based on the Parratt formalism [13], [15], [16]. The reflectivity amplitude R for a layer with index i can be obtained by:

$$R_i = a_i * \frac{R_{i+1} + f_i}{R_{i+1} * f_i + 1} \tag{2.6}$$

With a_i being the phase factor and the index i+1 describing the layer below,

$$a_i = e^{-2ik_i d_i} \tag{2.7}$$

k_i describing the normal component of the wavevector, d_i as the layer thickness and the Fresnel coefficient f_i.

$$f_i = \frac{k_i - k_{i+1}}{k_i + k_{i+1}} \tag{2.8}$$

After recursion the total reflectivity can be obtained through the complex modulus of the reflectivity amplitude at the surface of the first layer: [16]

$$R_{total} = \left|R_0^2\right| \tag{2.9}$$

Software Comparison

Stochfit performs a model independent fit of the reflectivity curve that leads to an electron density profile (EDP). Starting parameters for this are an estimation of the film thickness as well as an average scattering length density (SLD) of the film as well as the substrate, that can be obtained through a built-in SLD calculator. The scattering length density is a quantity used to describe the scattering power of a given material described in (2.10) [16].

$$SLD = \frac{r_e N_A \rho}{M} \sum_{i=1}^{N} f_i \tag{2.10}$$

Here r_e describes the classical electron radius, N_A is Avogadro's number, ρ is the density of the given material, M the molecular weight, N the number of atoms and f_i the real anomalous scattering factor of an atom i [16].

In addition, the film needs to be divided into a number of equidistant boxes. Typically, 1.5 – 2 boxes per Angstrom in film thickness are ideal. The software then performs an EDP search and tests in case of the standard "greedy search" program via a fitness function if the obtained reflectivity fit is acceptable. Additionally, a simulated annealing algorithm also exists to find the global minimum, since no unique EDP exists for an XRR-curve. Although it is possible to find the global minimum with simulated annealing, the solution depends on the initial temperature as well as the cooling schedule [16].

In comparison X'Pert Reflectivity performs a model dependent fit. For this a starting model of homogeneous layers needs to be set. The software then calculates density, layer thickness and roughness for these layers within certain boundaries.

X-Ray Diffraction

X-ray diffraction is an integral characterisation method for the determination of the molecular packing within a crystalline solid. It is based on the principal that an incoming X-ray beam penetrates a sample and is elastically scattered by the electron-cloud, which forces the electrons to oscillate approximately like a dipole, emitting dipole radiation. During this scattering event, called Thomson scattering, the wavelength is preserved. In crystalline structures diffraction of the outgoing beam occurs since the interatomic distance and the wavelength of X-rays are in the same order of magnitude and the crystal acts as a lattice. In real space this is described by the Bragg condition:

$$n\lambda = 2d_{hkl} * \sin\vartheta \tag{2.11}$$

With n being the order of diffraction, λ the wavelength, d_{hkl} the interplanar distance with hkl as integers and θ as half of the scattering angle.

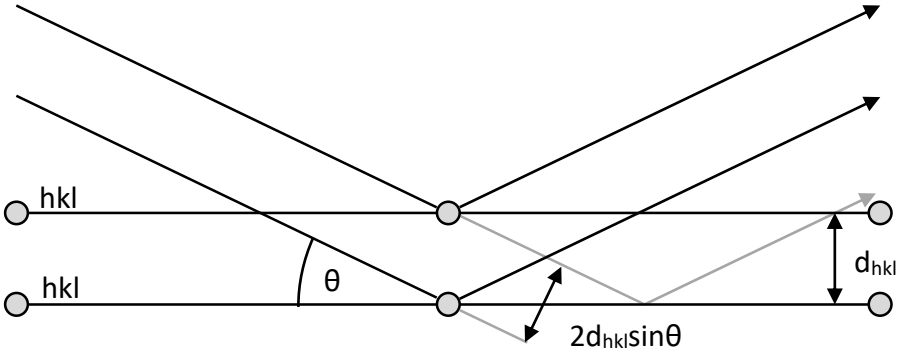

Fig. 12: Schematic illustration of Bragg's law [23]

This can also be described in reciprocal space by the Laue condition, which describes that for diffraction to occur the wavevector **q** needs to equal the reciprocal lattice vector **G**:

$$\boldsymbol{q} = \boldsymbol{G_{hkl}} \tag{2.12}$$

With the wavevector **q** being the difference between the incoming wave $\mathbf{k_0}$ and the outgoing wave **k**

$$\boldsymbol{q} = \boldsymbol{k} - \boldsymbol{k_0} \tag{2.13}$$

And **G** described by the Miller indices hkl and the primitive vectors **a***, **b*** and **c***:

$$\boldsymbol{G_{hkl}} = h\boldsymbol{a}^* + k\boldsymbol{b}^* + l\boldsymbol{c}^* \tag{2.14}$$

Since the lattice of a thin film is not infinite, the slit interference function should also be considered to determine size effects of the lattice:

$$L(\boldsymbol{qa}) = \frac{\sin^2(\frac{\boldsymbol{qa}N}{2})}{N^2 * \sin^2(\frac{\boldsymbol{qa}}{2})} \tag{2.15}$$

With **q** being the wavevector, a the interplanar distance and N the number of repeating units. The function can be used to obtain the number of repeating units in q- direction, the length of the unit cell in this direction and most importantly the thickness of the layer creating Bragg peaks in a specular measurement.

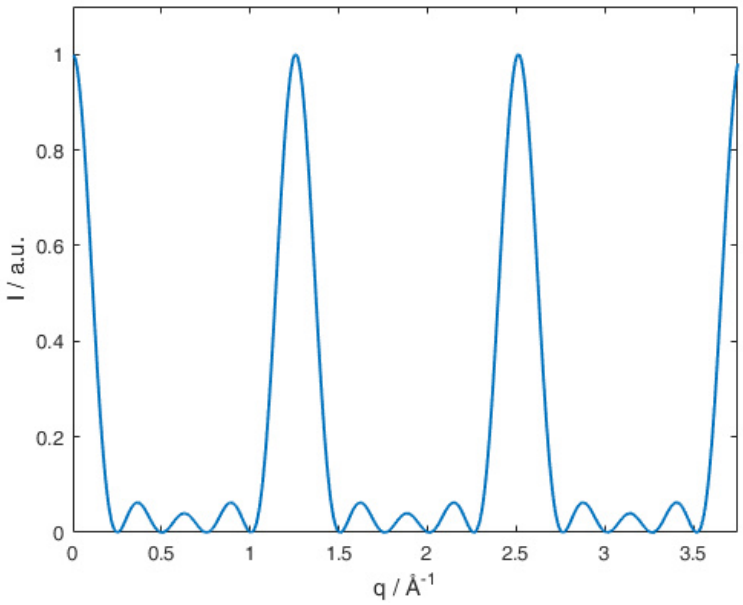

Fig. 13: Illustration of the Slit Interference Function for the case of N = 5 and a = 5 Å with a indicating the position of the main-peaks and N influencing the number of sidepeaks

In this thesis specular X-ray diffraction as well as grazing incidence X-ray diffraction were used to characterise the films.

Specular X-Ray Diffraction

Specular x-ray diffraction describes a technique, in which the angle between the incident beam and the substrate and between the diffracted beam and substrate are equal. This leads to the wavevector always being orthogonal to the substrate surface which means that out-of-plane information can be obtained.

During a specular measurement the incidence angle is steadily increased, while the detector is moved at the same time to maintain the specular condition. This leads to the wavevector being perpendicular to the substrate and only increasing in length.

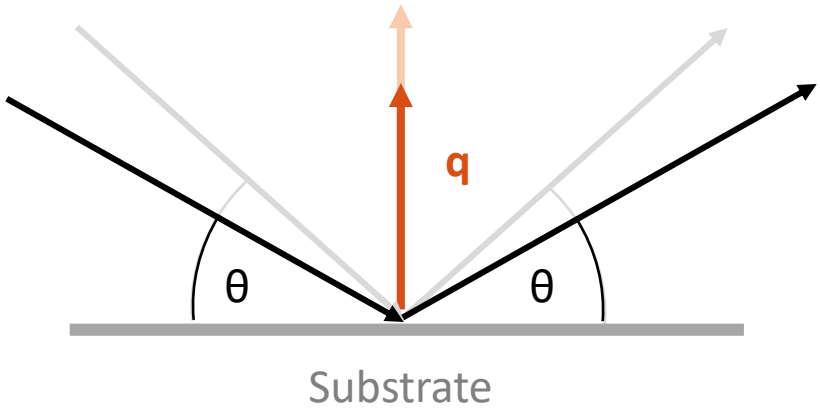

Fig. 14: Illustration of the specular condition with the angle of the incoming and outgoing beam being equal and the wavevector scaling with the incidence angle

As for XRR, the measurements were performed with a Panalytical Empyrean, with the setup only slightly differing. On the side of the incident beam a 1/8° slit was mounted, while on the detector side a 7,5 mm anti-scatter slit was placed. Another difference to XRR was the measured range with incidence angles between 5° and 30° and a 1D-detector was used.

Grazing Incidence X-Ray Diffraction

Grazing incidence X-ray diffraction (GIXD) is a technique in which an incoming beam with an incidence angle close to the critical angle of total reflection is reflected off a sample. During this an evanescent wave is created at the surface that oscillates parallel to the surface and can be used for diffraction. In contrast to specular X-ray diffraction also planes non-parallel to the substrate can be investigated, which means that the wavevector is no longer orthogonal to the surface and has a q_{xy} component in addition to the q_z part.

$$q_{xy} = \sqrt{q_x^2 + q_y^2} \tag{2.16}$$

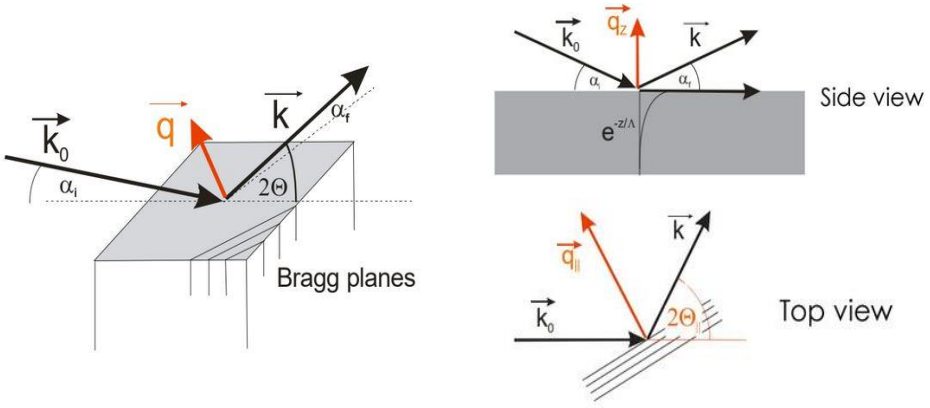

Fig. 15: Schematic represantation of the beam path as well as the orientation of the wavevector during GIXD – experiments [21]

Furthermore, it has to be noted, that GIXD is a surface sensitive technique since the evanescent wave decays exponentially into the sample and the penetration depth can be changed by changing the incidence angle. In addition, the intensity of the evanescent wave reaches a maximum at the critical angle, which means that the detected intensity of the investigated Bragg peak also increases at grazing incidence angles. The critical angle α_c is the lowest angle at which X-rays can penetrate the sample surface.

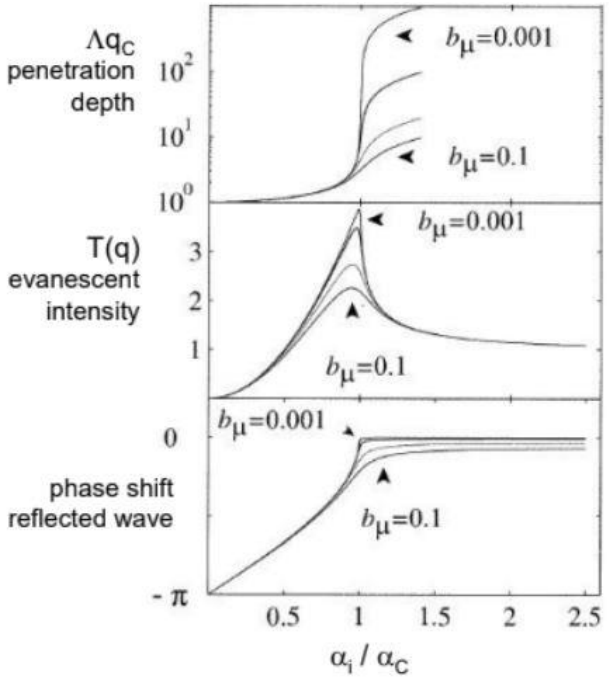

Fig. 16: Penetration depth, intensity of the evanescent wave and phase shift of the reflected wave around the critical angle of total reflection [21]

All grazing incidence X-ray diffraction experiments in this thesis were performed at the XRD1 beamline of Elettra Sincrotrone Trieste. The light source of this beamline is a multipole wiggler with a range from 4 to 21 keV. The components of the beam optics are a vertical collimating mirror, a double-crystal Si (111) monochromator and a bendable toroidal focusing mirror. The measurement setup consists of a Huber Kappa Goniometer and a Pilatus 2M detector [17]. For measurements the samples were aligned through a laser-alignment process. The wavelength used during experiments was 1,4 Å.

Results and Discussion

Sub-Monolayer and Monolayer Coverages

Atomic Force Microscopy

Samples with a nominal layer thickness of 20 - 30 Å show the formation of plateau-like islands with a surface coverage of 40 – 50%. Through a linescan across one of these islands an island-height of 55 Å can be determined. This can be verified by the height distribution in Fig. 18, which shows two distinct peaks separated by a distance of 55 Å. This height is in agreement with the length of the long unit cell axis in the bulk structure as well as the height of two upright standing molecules on top of each other. In addition, analysis of a phase image shows a clear phase-shift between the islands and the area in between, which can be an indicator for a change in material.

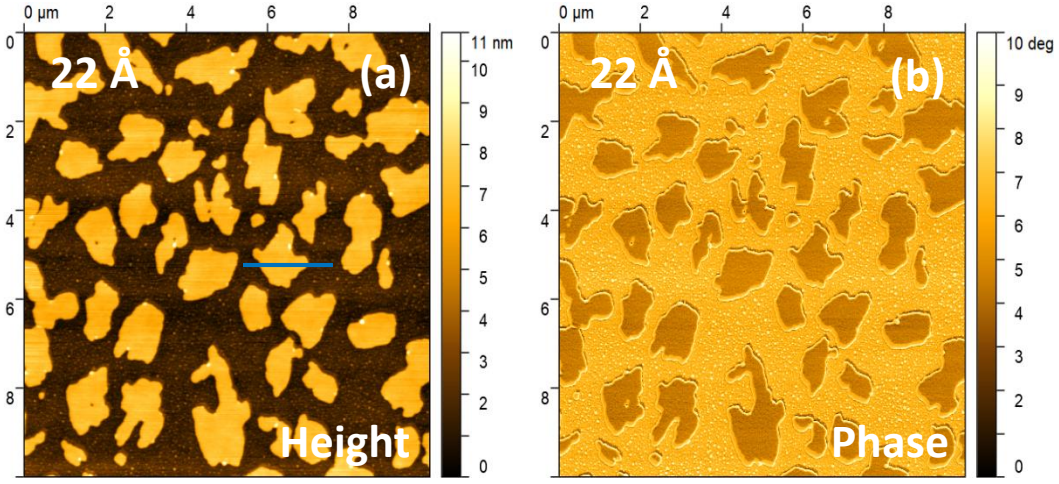

Fig. 17: Height image (a) as well as phase image (b) of a 22 Å nominal thickness sample with the position of the linescan in Fig.18 indicated by the blue line

The phase shift in Fig. 17 (b), in conjunction with the nominal layer thickness of approximately 20 Å and the island height of 55 Å, indicates that the first two layers of the organic film form double-layer islands with the Si/SiO_2 substrate in between.

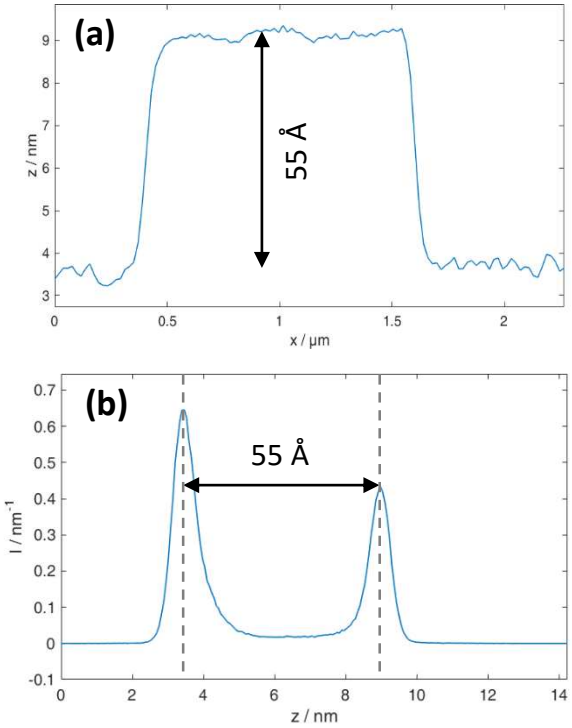

Fig. 18: Height profile (a) of a linescan indicated in Fig.17 as well as the height distribution (b) of the same image

Samples with a nominal film thickness of 50 – 60 Å exhibit an increased double-layer coverage of about 90 %. In addition, the development of a third layer on top of the existing structure, as well as the formation of bigger crystallites, with heights ranging from approximately 100 Å to 150 Å, is observed. In the area surrounding these crystallites the substrate is visible and the aforementioned double-layer structure disappears as can be seen in Fig. 19 (a). The height of the double-layer structure is 43 Å according to Fig.19 (b) with height steps between additional layers being 23 – 24 Å. The reduced heights compared to the expected values of 53 Å for the double-layer as well as 27 Å for additional layers can be explained by interaction between the AFM tip and the organic film.

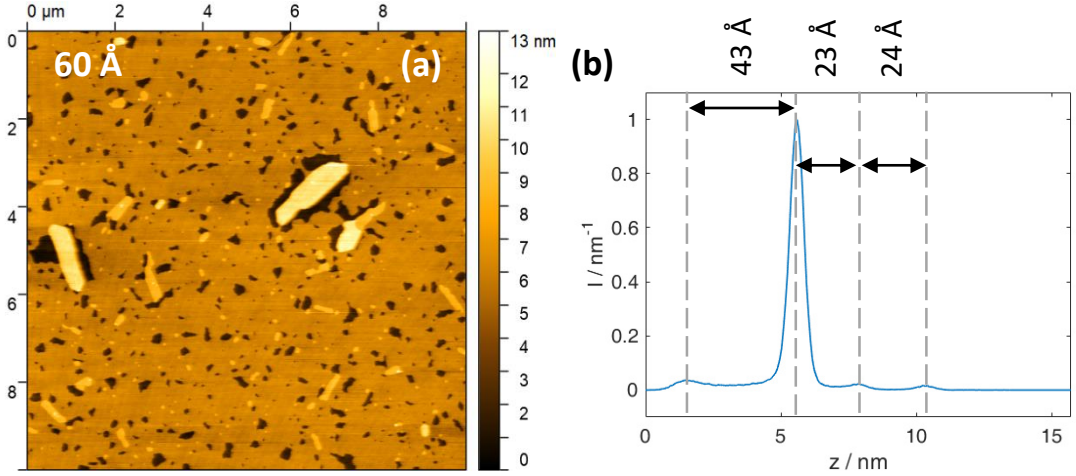

Fig. 19: Atomic force microscopy image of a sample with a nominal thickness of 60 Å (a) and the height distribution of this image (b)

X-Ray Reflectivity

Atomic force microscopy images of samples with nominal thicknesses ranging from 20 Å to 60 Å show no significant difference in film thickness but mainly differ in surface coverage instead. This is validated by X-Ray reflectivity measurements of samples with these nominal thicknesses. Fig. 20 shows that the width of Kiessig fringes doesn't vary between the two curves, which indicates, that the film thickness is identical. The measurements only differ in how well defined the fringes are, which indicates a difference in electron density between the samples.

This is explained by a difference in surface coverage between those samples, which is in agreement with the results obtained by atomic force microscopy.

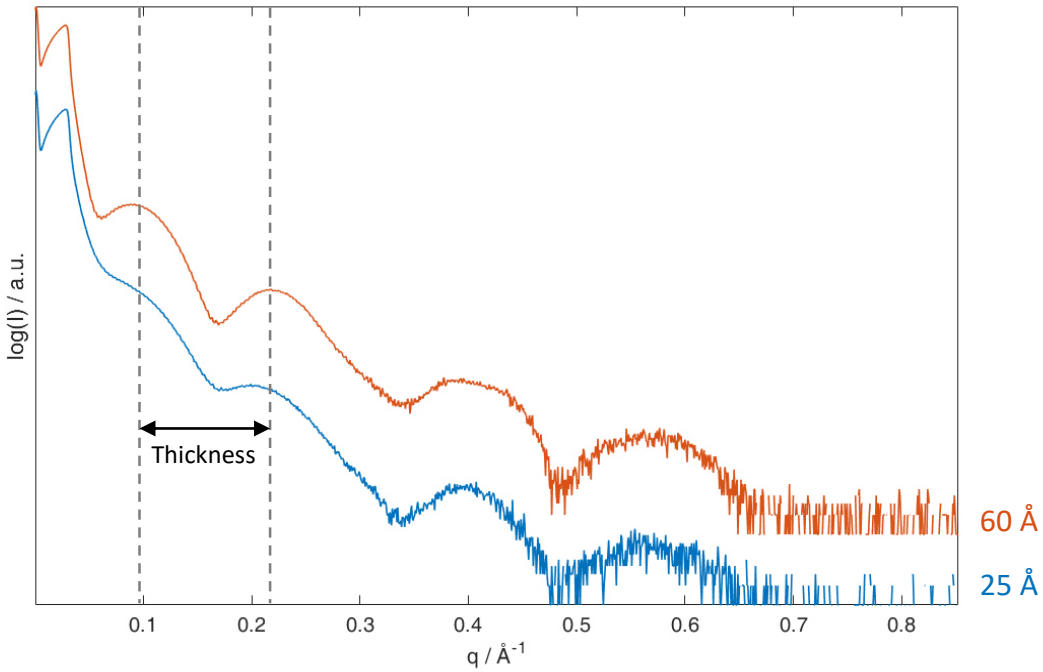

Fig. 20: Comparison of the X-Ray reflectivity curves for a nominal 25 Å sample and a nominal 60 Å sample, the identical broadness of the Kiessig fringes indicates them having the same film thickness

X-ray Reflectivity - Data Evaluation

For a more accurate determination of the film parameters, a fit of the measured reflectivity curve needs to be performed. This was done on a sample with a nominal film thickness of 50 Å, since it exhibits a nearly closed molecular double layer.

Fig. 23 shows a fit performed with the software X'Pert Reflectivity, where a model with a tail-to-tail arrangement of two molecules on top of each other with the Phenylgroups sticking outwards was used. Although the fit doesn't follow the measured data perfectly, it gives first insights into the arrangement of molecules in the film. This can be further supported, by comparing the fit to fits performed with different models, like in Fig. 21, where a head-to-head arrangement with the Decylchains sticking outwards is used.

The lengths of both Core- and Phenyl-layers obtained through the fit in Fig. 23 match well with the expected layer thickness of 15,9 Å. In contrast, the lengths of the Decylchains deviate from the expected result of 10,5 Å, but sum up to the expected length of two Decylchains stacked on top of each other. This can be caused by the presence of two layers of the same material stacked on top of each other, which hinders an accurate fit of the layer thickness due an absence of a significant change in electron density between those layers. In addition, the

densities of the layers in Fig. 23 are lower than the expected values for a surface-coverage of 90 % of approximately 1,2 g/cm³ for the Core- and Phenyl-layers as well as 0,9 g/cm³ for the Decylchains.

Through the GIXD measurement in the next chapter, it can be seen that those two models are the only possibilities for molecular arrangement, because the samples exhibit the known crystal structure.

The fit in Fig. 21 doesn't follow the measured data and the used model differs significantly from reality, because a higher density of the sidechains than the BTBT-cores as well as a layer roughness higher than the layer thickness are physically impossible. This in conjunction with the fact, that the models used in Fig. 21 and Fig. 23 are the only possible solutions, makes a tail-to-tail arrangement the most likely model.

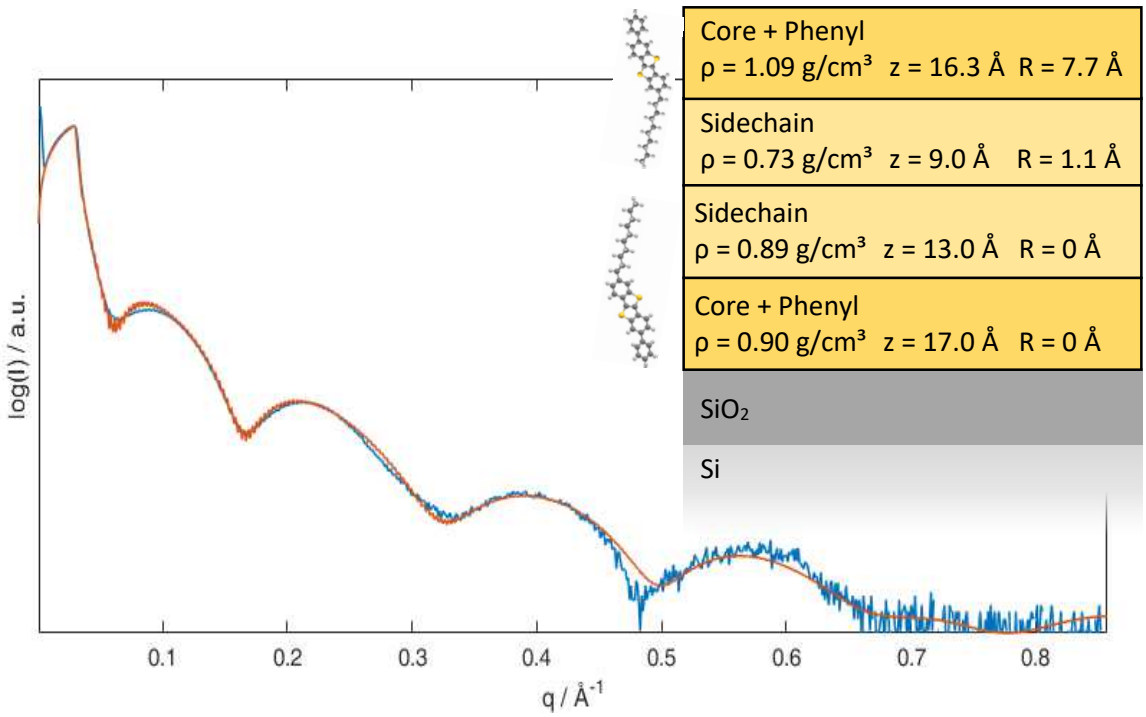

Fig. 23: XRR fit of a nominal 50 Å sample (orange) determined through X'Pert Reflectivity with the measured curve (blue) and the model used for fitting in the top right corner

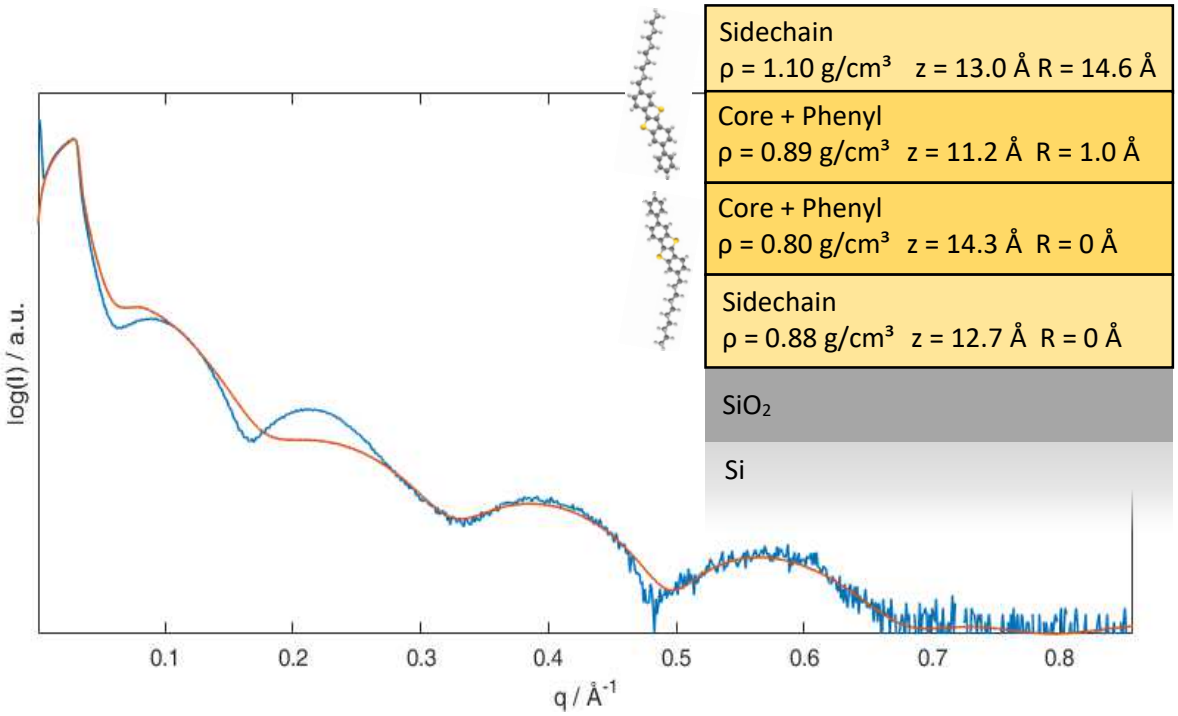

Fig. 21: XRR fit of a nominal 50 Å sample (orange) determined through X'Pert Reflectivity with the measured curve (blue) with an alternate model used for fitting in the top right corner

For further investigation a model independent fit was also performed. Therefore, a “greedy search” [16] as well as simulated annealing were used to ensure that the obtained result is as likely as possible. Both model independent fits show an increased electron density of the film at the interface with the substrate as well as at the film surface with lower density in between. The fits with both search algorithms follow the measured data well, although the obtained electron density distribution deviates from the expected model in some points. Generally, the results of both model independent fits point towards a tail-to-tail arrangement, although the electron density doesn’t fit perfectly.

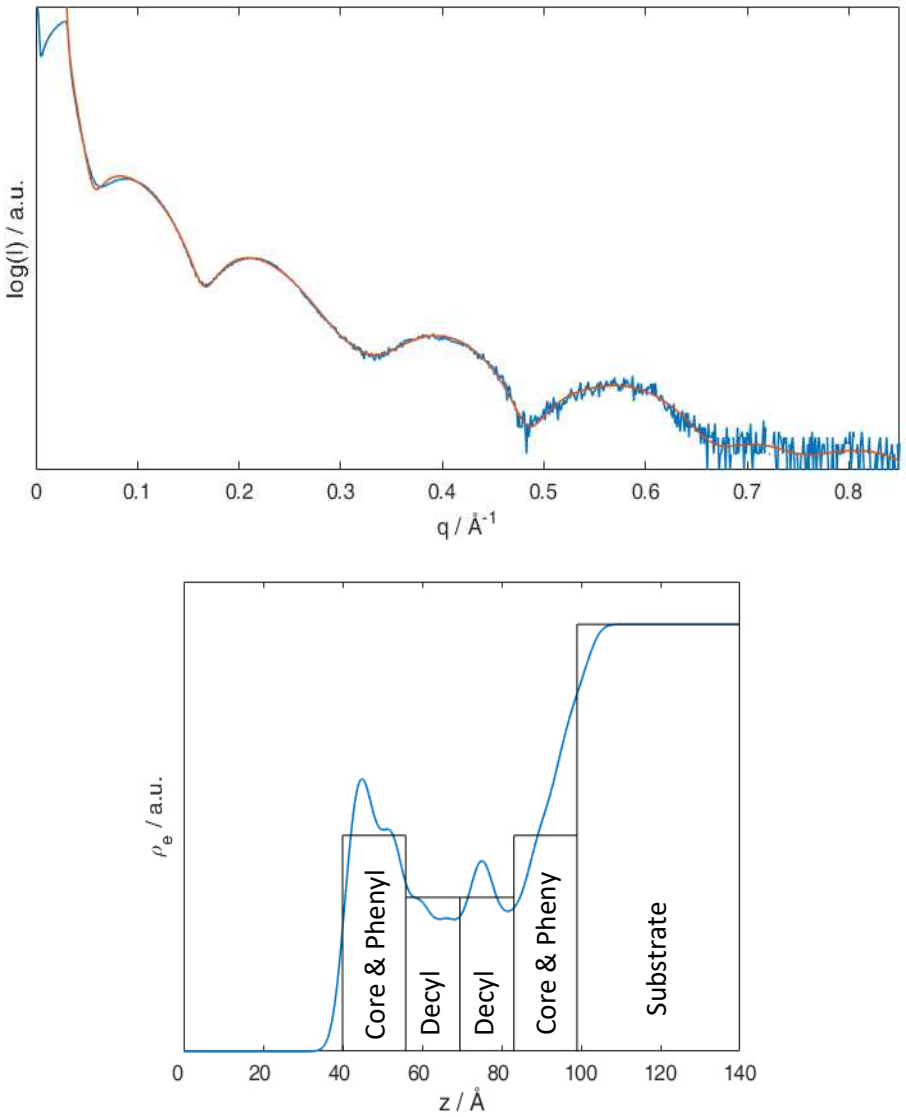

Fig. 24: Measured reflectivity curve (top blue) of a sample with nominal thickness of 50 Å with a model independent fit (top orange) obtained through the "greedy search" algorithm and the electron density distribution of this fit (bottom blue) with an estimated model (bottom black)

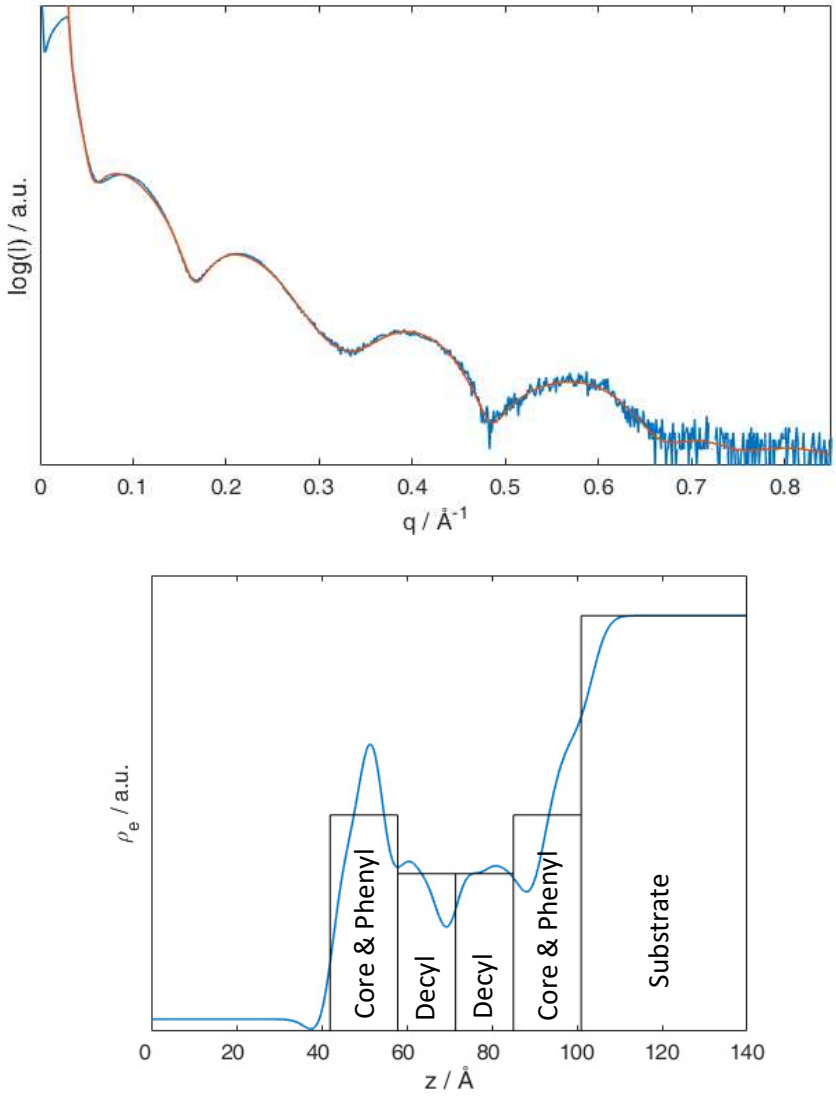

Fig. 25: Measured reflectivity curve (top blue) of a nominal 50 Å sample with a model independent fit (top orange) obtained through simulated annealing and the electron density distribution of this fit (bottom blue) with an estimated model (bottom black)

When summarising the results of the X-ray reflectivity fits, it can be assumed, that the first two molecular layers grow in a tail-to-tail arrangement with the Phenylgroups pointing outwards. Alternate models for the model dependent fit yield suboptimal results, that are physically impossible or break down during the fitting process and don't follow the measured XRR curve. Model independent fits mostly result in the model described in Fig. 24 and Fig. 25. Alternative results lead to electron density distributions that can either be interpreted by multiple different models or are impossible to interpret with a solution that is in agreement with the results of grazing incidence X-ray diffraction measurements.

Grazing Incidence X-Ray Diffraction

In addition, grazing incidence X-ray diffraction was performed to determine the crystal structure of these films. The sample in Fig. 26 was measured with an incidence angle of 0,15°, which is below the critical angle of total reflection of Si as well as SiO_2. In both of these materials the critical angle lies at approximately 0,22°, while the critical angle of the organic film is at about 0,17°. The measurement was performed in this way to obtain a reduced penetration depth into the substrate as well as an increased intensity of the signal measured from the organic film. This is caused by the fact that the signals of the SiO_2 layer and the 11l rod of the Ph-BTBT-10 film overlap. Through this method, the signal from the substrate was reduced, while the signal intensity of the film was enhanced.

As can be seen in Fig. 26 on a sample with a nominal thickness of 22 Å as well as a sample with a film thickness of 54 Å the peak positions as well as the intensities are in agreement with the size of the unit cell as well as the structure factor of the known phase. This matches with the results of the X-ray reflectivity fits of these samples, where the model obtained by the reflectivity fits can be interpreted with the known crystal structure.

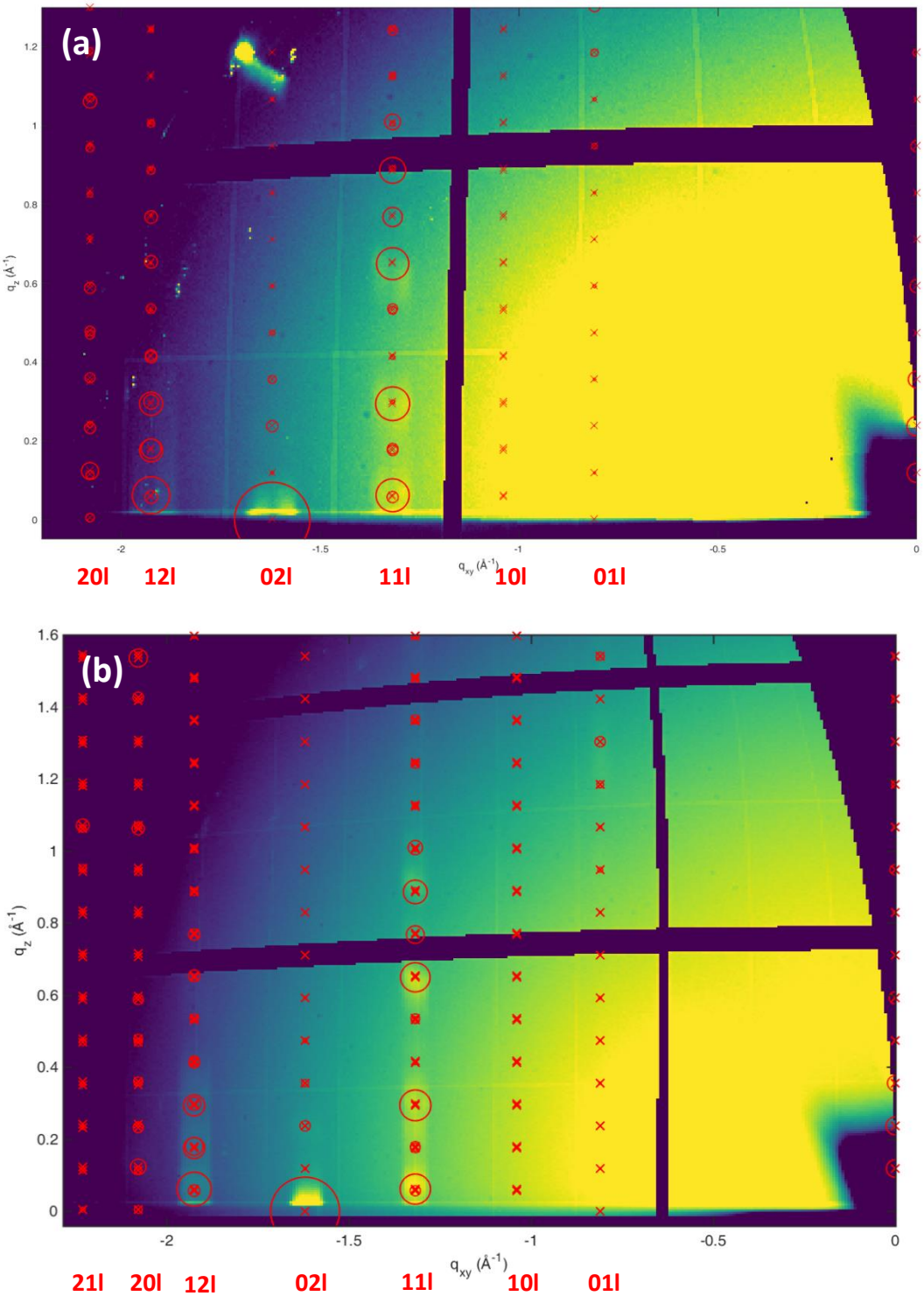

Fig. 26: Grazing incidence X-ray diffraction images of a nominal 22 Å sample measured with an incidence angle of 0,15° (a) as well as a sample with a film thickness of 54 Å measured with an incidence angle of 0,2° (b), peak positions and structure factors of the known crystal structure are indicated by red markers

Intermediate Film-Thicknesses

Atomic Force Microscopy

Samples with film thicknesses from 69 Å to 81 Å exhibit an increase in the amount of bigger crystallites as well as an increase of crystallite size compared to 50 Å and 60 Å samples. Furthermore, the first two layers still form a double-layer with a third layer with increased coverage compared to Fig. 28 (a) growing on top. In addition, the formation of a fourth layer can be observed. Overall a roughening of the film with increasing nominal film thickness is observed as the film transitions from a nearly flat double layer to a third as well as a fourth layer with low coverage growing on top.

A significant change in the morphology can be observed for samples with nominal film thickness of more than 107 Å. The crystallites decrease in size with increasing film thickness and disappear at thicknesses of more than 177 Å. In addition, the morphology of the top layer changes and lamellar islands are observed. With a further increase in layer thickness this structure change becomes more apparent, the crystallites have disappeared and the lamellar structure is fully visible.

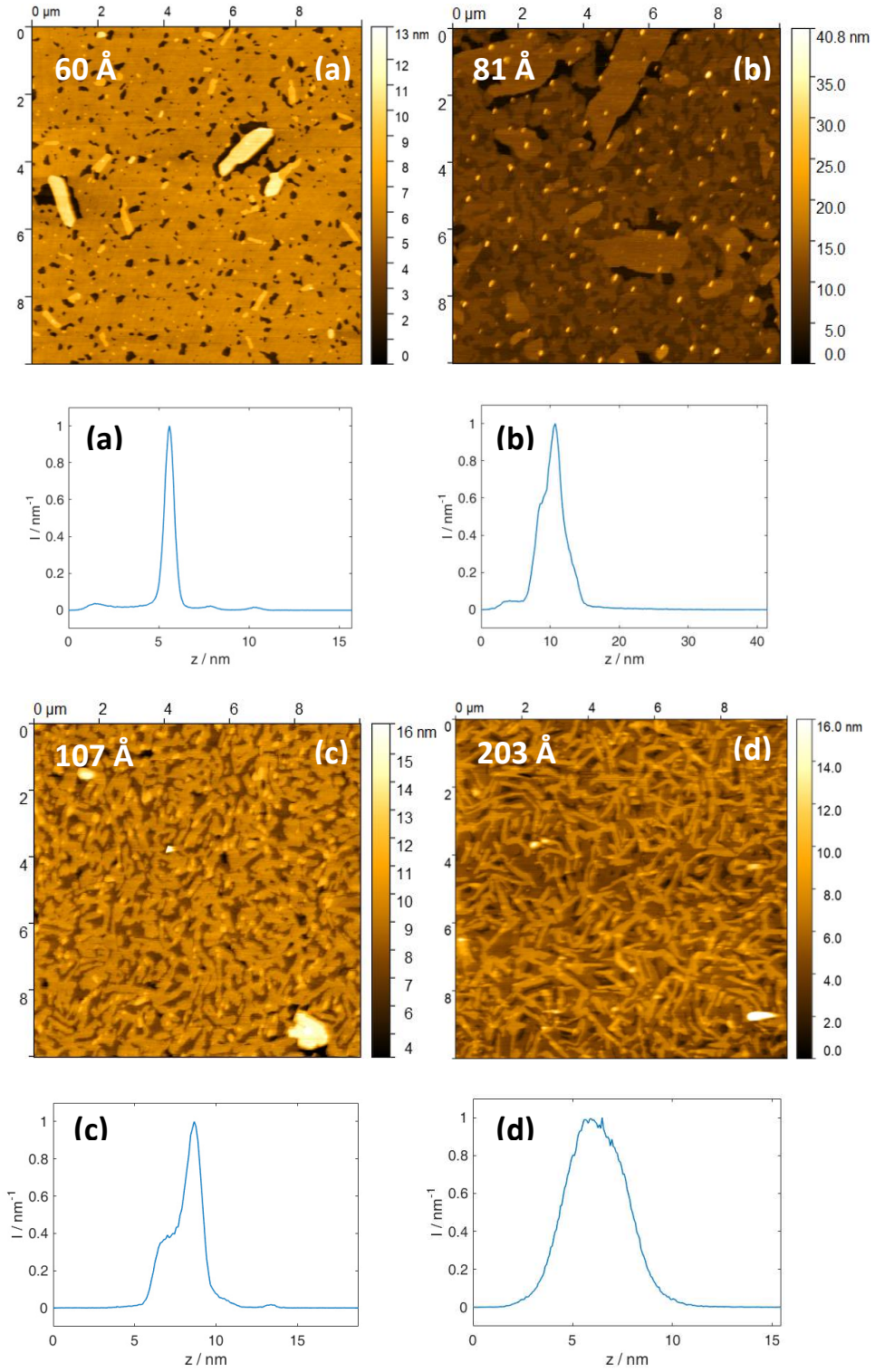

Fig. 28: AFM images and height distribution functions of a sample with a layer thickness of 60 Å (a), a 81 Å sample (b) and a sample with 107 Å thickness (c), as well as a 203 Å sample (d), the dots in (b) are a measurement artifact

X-Ray Reflectivity

X-ray reflectivity measurements of samples with a nominal layer thickness of approximately 54 Å show no Bragg peaks with an observable intensity. In contrast, to that samples with a film thickness of 69 Å as well as 81 Å show Bragg peaks with low intensity, that interfere with Kiessig fringes at the positions of the 001, 002, 003 and 005 peaks of the bulk phase. When comparing the structure factor of the bulk phase, pictured in Fig. 30, with the presence of these peaks, this indicates that the known crystal structure is present in those samples.

In contrast to that Bragg peaks appear in samples with a thickness of more than 107 Å at the positions of the 002, 004 and 006 bulk peaks. This can't be explained by the known structure anymore and indicates a change in crystal structure with a new structure that has similar peak positions as the crystal structure observed in thinner films, but differs in peak intensities. With increasing film thickness, the Bragg peaks become more apparent at the positions of the 002, 004 and 006 bulk peaks with the odd numbered peaks being absent, which indicates a change in crystal structure.

This change follows a transformation of the morphology that was already seen in the atomic force microscopy images and can be seen at the same film thickness, were the morphology changes from a double layer with crystallites growing in between to the formation of elongated islands.

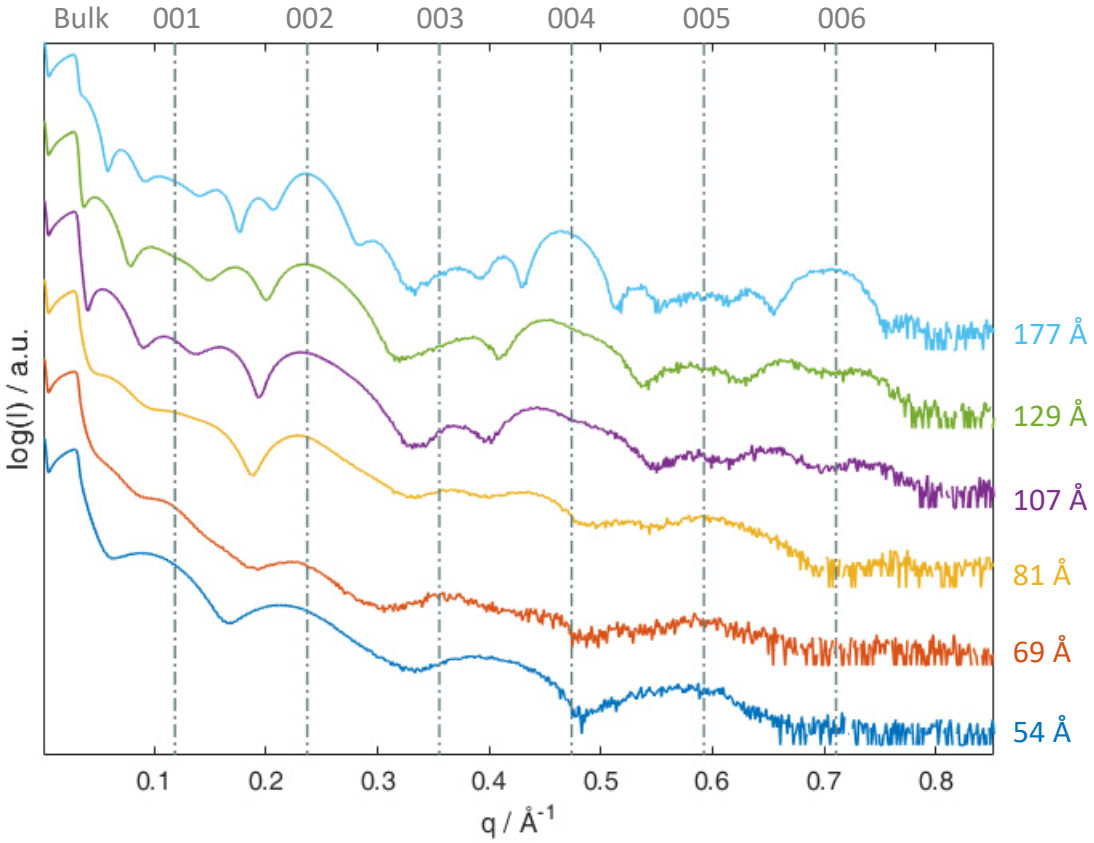

Fig. 29: X-ray reflectivity curves of samples with increasing thickness and peak positions of the known bulk phase indicated by grey lines

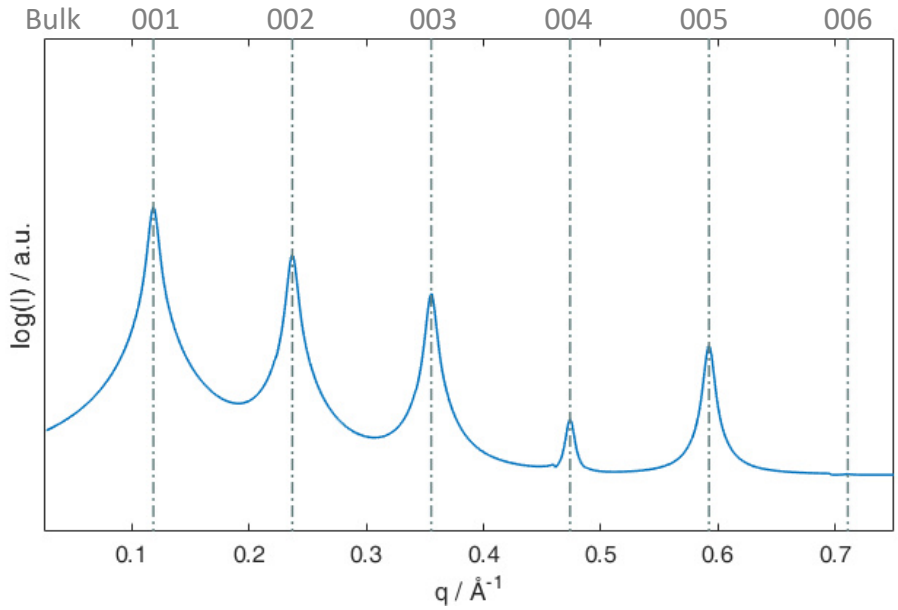

Fig. 30: Peak intensities/structure factor for the known bulk crystal phase

Grazing Incidence X-Ray Diffraction

Samples with a layer thickness up to 81 Å match in peak intensity with the known crystal structure, as can be seen in Fig. 31 (a). In contrast to that a linescan in Fig. 32 indicates, that the measured peaks are shifted compared to the positions of the bulk phase. This contradicts the results obtained by X-ray reflectivity and the results of the grazing incidence diffraction images of samples with layer thicknesses of 22 Å and 54 Å in Fig. 26.

The measurement of a sample with a film thickness of 107 Å shows peaks, that are slightly shifted relative to the peak positions of the known phase, indicated in Fig. 31 (b). In addition, the peak intensities of the 111 and the 112 peak in particular don't match the expected intensities.

This further indicates a change in crystal structure, which is observed at the same film thicknesses here as in the reflectivity and atomic force microscopy measurements. This caused the development of a new unit cell, that can be seen in Fig. 29 (b) and is further described later in Table 2.

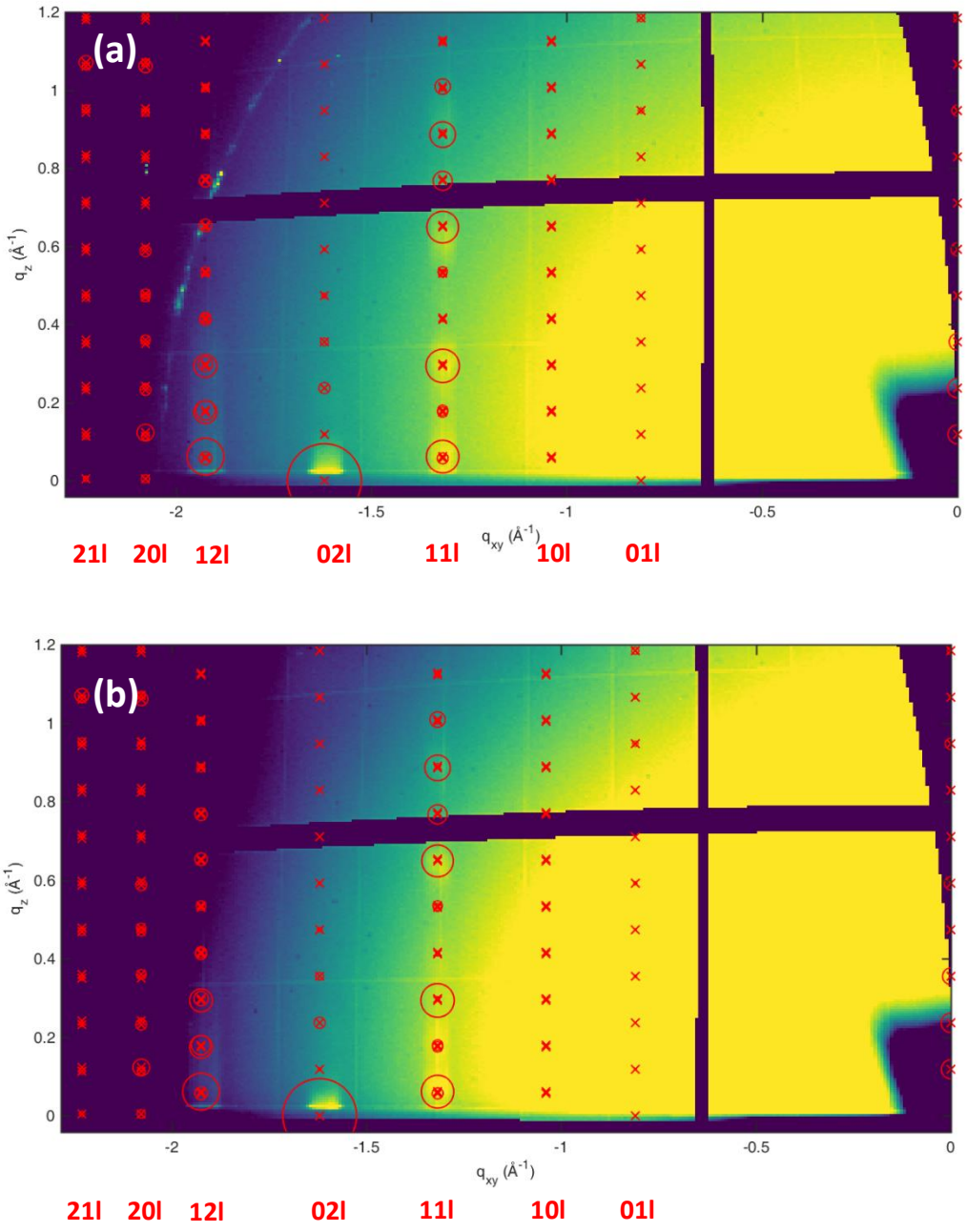

Fig. 31: Grazing incidence X-ray diffraction images of a sample with a film thickness of 81 Å (a) and 107 Å (b) with peak positions and intensities of the bulk phase indicated in red

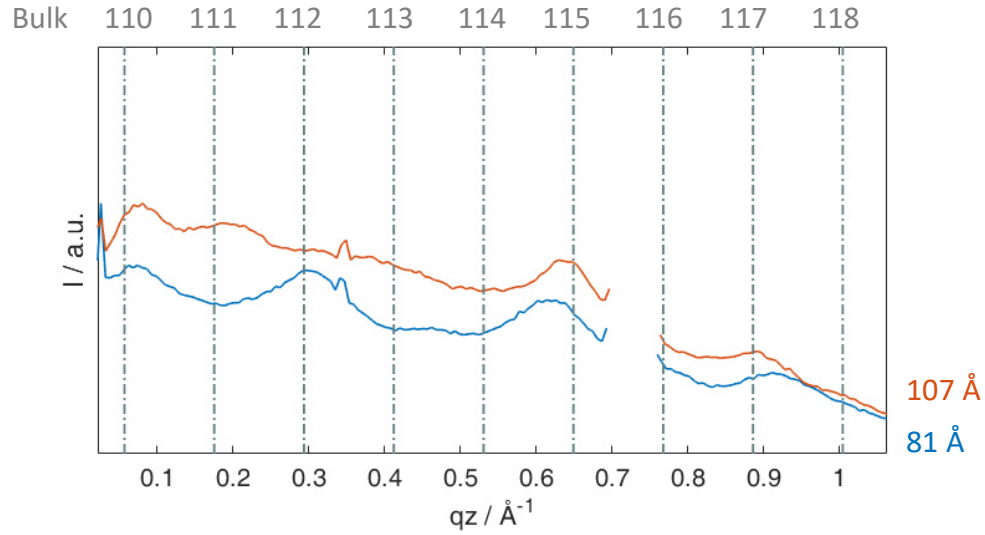

Fig. 32: Linescan of the 11l- rod of samples with a film thickness of 81 A and 107 A with the peak positions of the known bulk phase indexed in grey

Thickest Samples

Atomic Force Microscopy

Atomic force microscopy of a sample with a film thickness of 220 Å in Fig. 34 (a) shows an increased formation as well as roughening of the elongated islands, that are already observed in Fig. 28 for samples with a film thickness higher than 107 Å. In between these islands a more uniform structure is still visible for a film thickness of 220 Å, that disappears in Fig. 34 (b). With increasing film thickness the lamellar islands become more prevalent and further roughening of the film is observed. In addition, no clear steps in height are visible anymore at a film thickness of 484 Å. A linescan across one of these islands was therefore performed and indicated, that height differences within the islands still follow integer multiple steps of the length of upright standing molecules, indicating that no further structure change occurred.

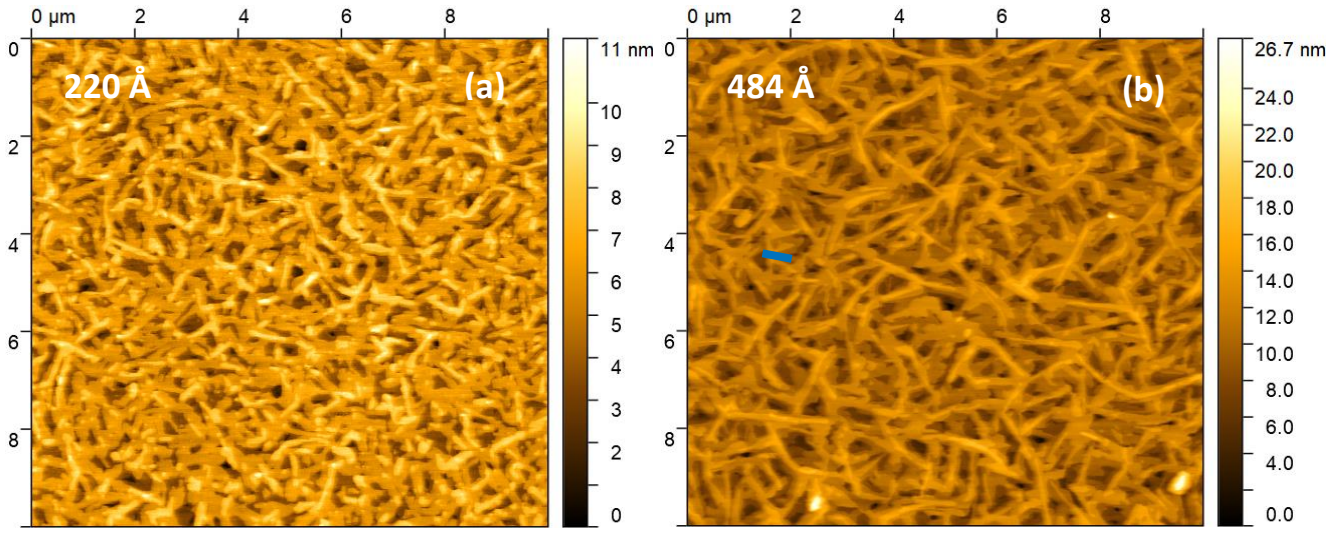

Fig. 34: AFM images of a sample with 220 Å film thickness (a) and a 484 Å sample (b)

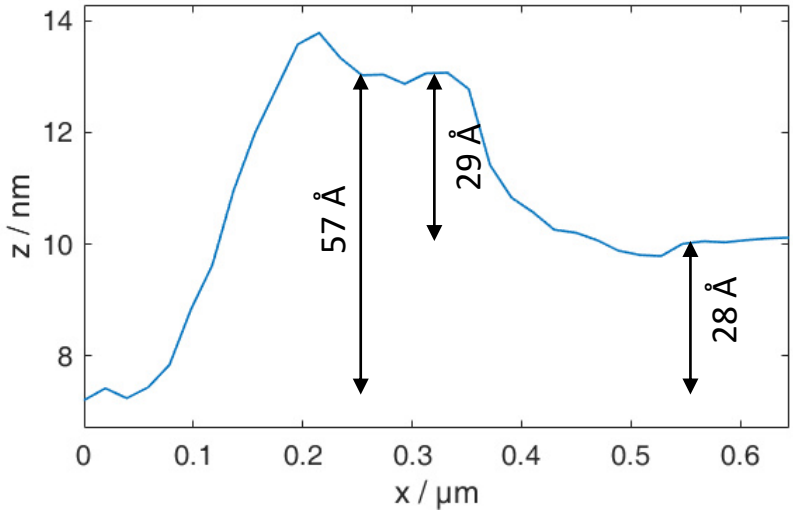

Fig. 33: Linescan across an island in Fig. 34 (b)

X-Ray Reflectivity

XRR curves of samples with a film thickness of more than 220 Å exhibit the absence of odd numbered peaks, already observed in Fig. 29 for samples with a thickness of more than 107 Å. In comparison to Fig. 29, the observed peaks in Fig. 35 are sharper, due to the increase in film thickness. This allows the evaluation of an increased peak shift with increasing incidence angle relative to the peak position of the known phase.

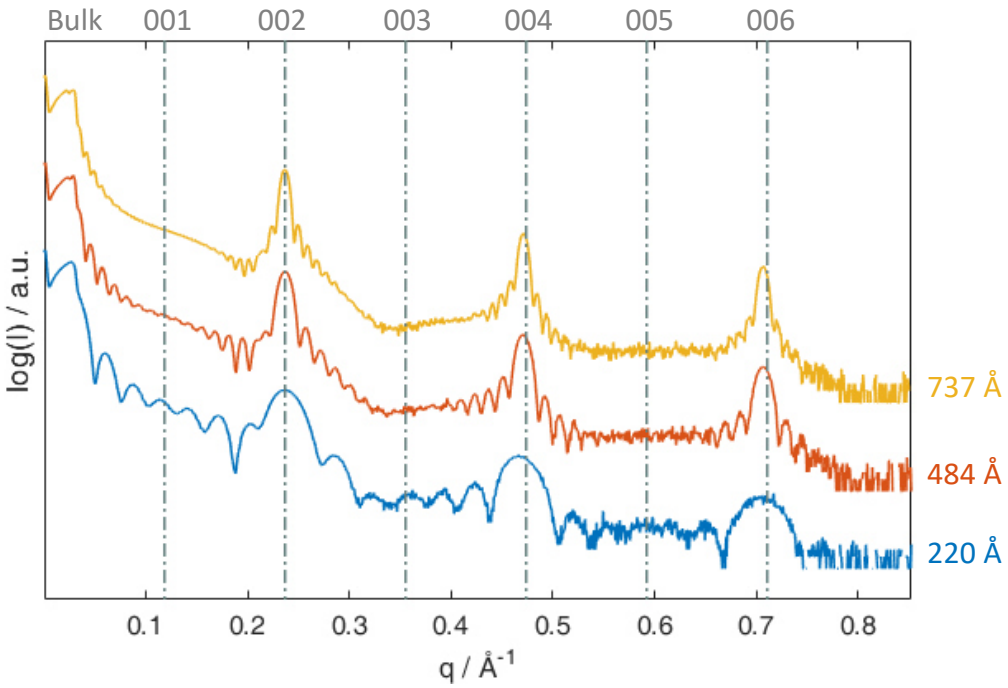

Fig. 35: XRR curves of samples with high film thicknesses with the peak positions of the known phase indicated by grey lines

This shift, together with the absence of odd numbered peaks in specular measurements as well as a change in peak intensity and a slight shift of the peak positions in grazing incidence diffraction measurements above a critical thickness, that are described in the previous chapter, further indicate the presence of a new crystal structure.

For further investigation the evaluation of these X-ray reflectivity curves was split into two methods, because fitting of the Bragg peaks with a reflectivity fitting software was impossible. X'pert Reflectivity was therefore used to fit the curve for low wavevectors to determine the film thickness and the Bragg peaks were evaluated through the slit interference function to determine the size of the crystallites causing them.

Layer Interference

The first few degrees of the X-ray reflectivity measurement were fit with a three-layer model, consisting of a contact layer at the interface with the substrate, a thicker layer to describe the bulk of the film and another thinner layer to account for film roughness, that is observed in the atomic force microscopy images. The fit follows the measured curve well and results in a film thickness of 484 Å, which is lower than the thickness of 582 Å measured in-situ during evaporation. Considering the preparation time of an hour and the fact, that the evaporation rate was only measured before and after preparation and interpolated, the difference in film thickness is negligible. In addition, the obtained film densities of 1,22 g/cm³ for the bulk layer and 1,20 g/cm³ for the contact layer match with the theoretical density of 1,22 g/cm³ with the density of the top layer being lower to account for lower coverage due to surface roughness and the formation of islands.

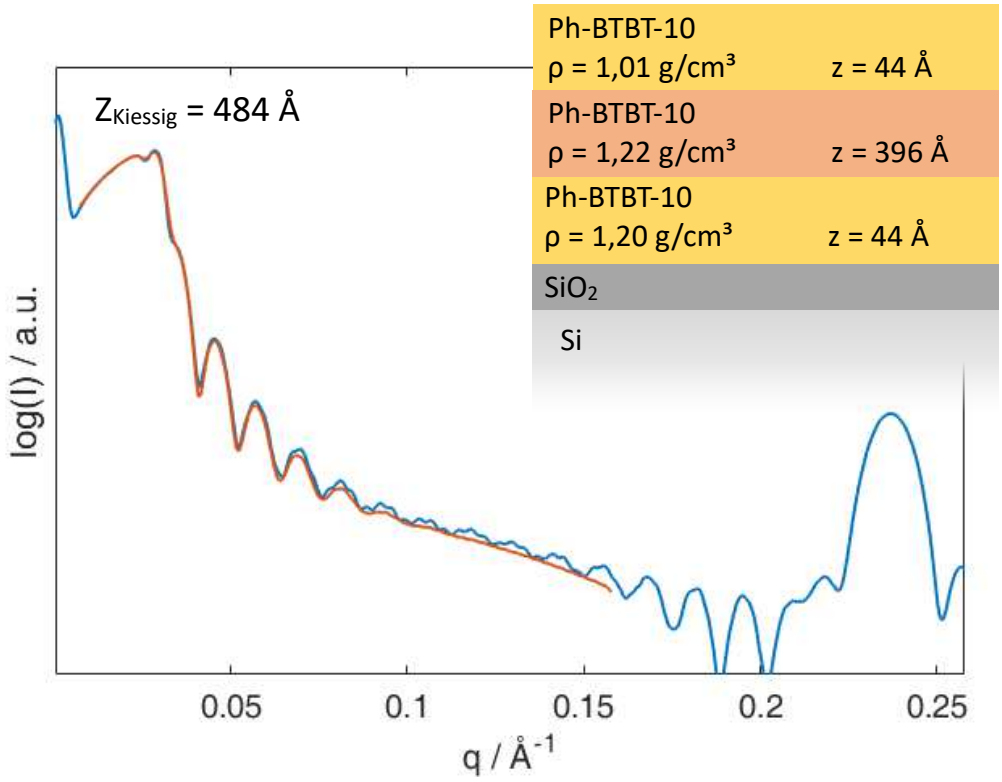

Fig. 36: XRR fit (orange) of a sample with a thickness of 484 Å and the model used for fitting

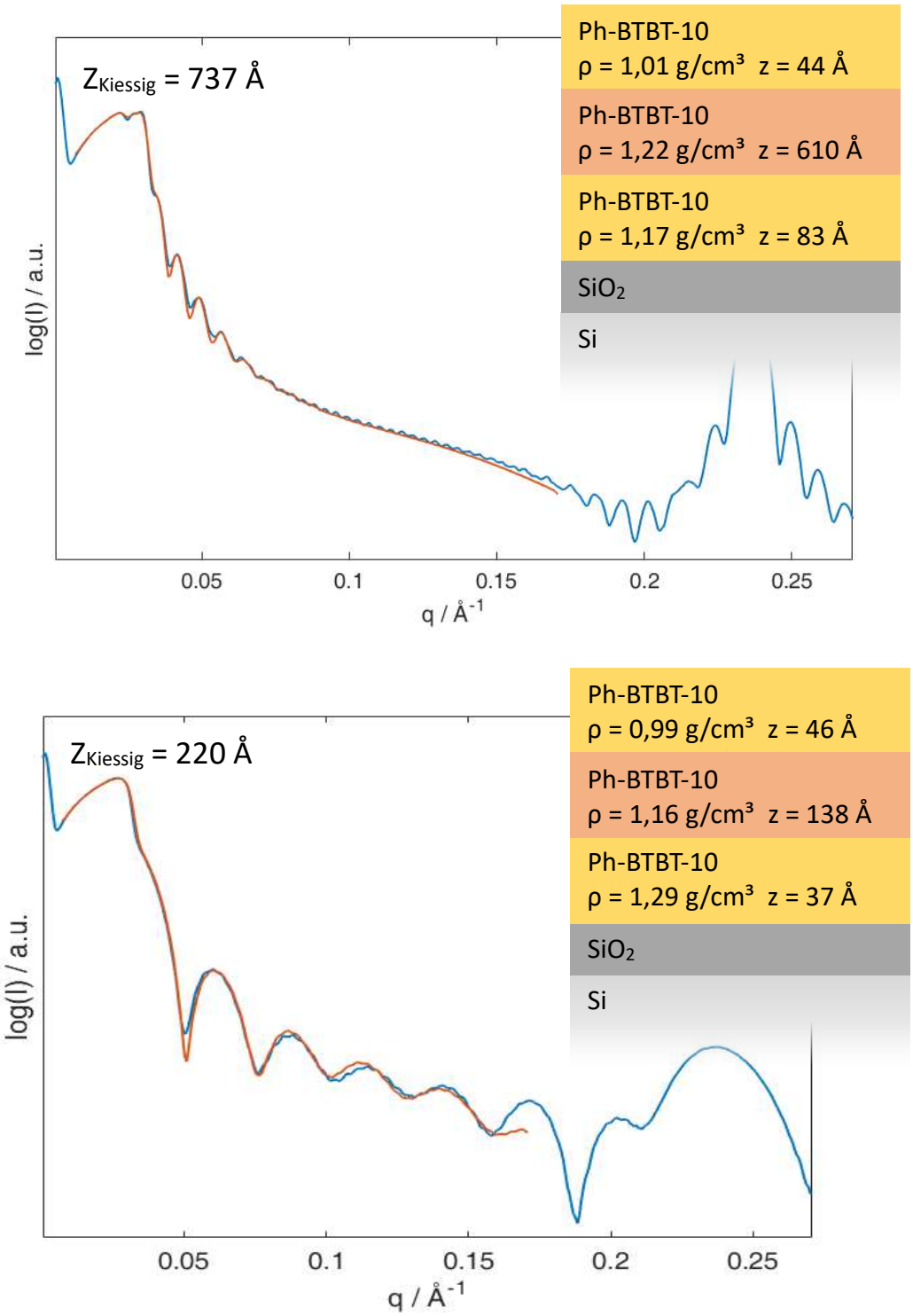

Fig. 37: XRR fits (orange) of samples with a film thickness of 737 A and 220 A with the model used for fitting

Slit Interference Function

In addition, the measured Bragg peaks were fit with the slit interference function. Besides slight differences at the side-maxima, caused by interference with Kiessig fringes as well as a negligible background due to film roughness, the fit matches the measured peak well.

The fit in Fig. 38 describes a model of 16 unit cells in specular direction, with a unit cell height of 26,7 Å orthogonal to the substrate. Through this model, a thickness of 427 Å perpendicular to the substrate can be obtained for the phase, that causes the Bragg peaks.

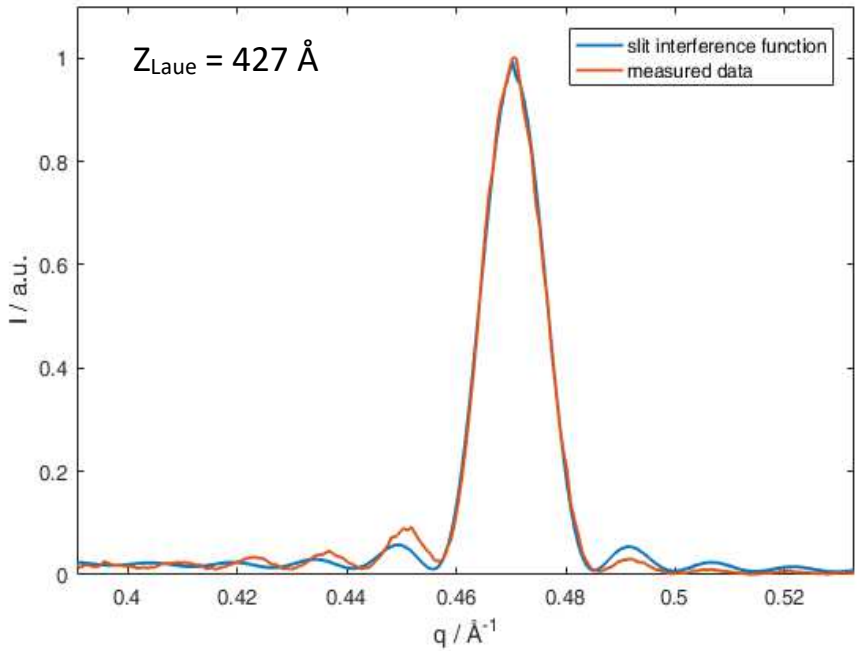

Fig. 38: Measured 002-peak of the new crystal structure as well as a fit obtained through the slit interference function

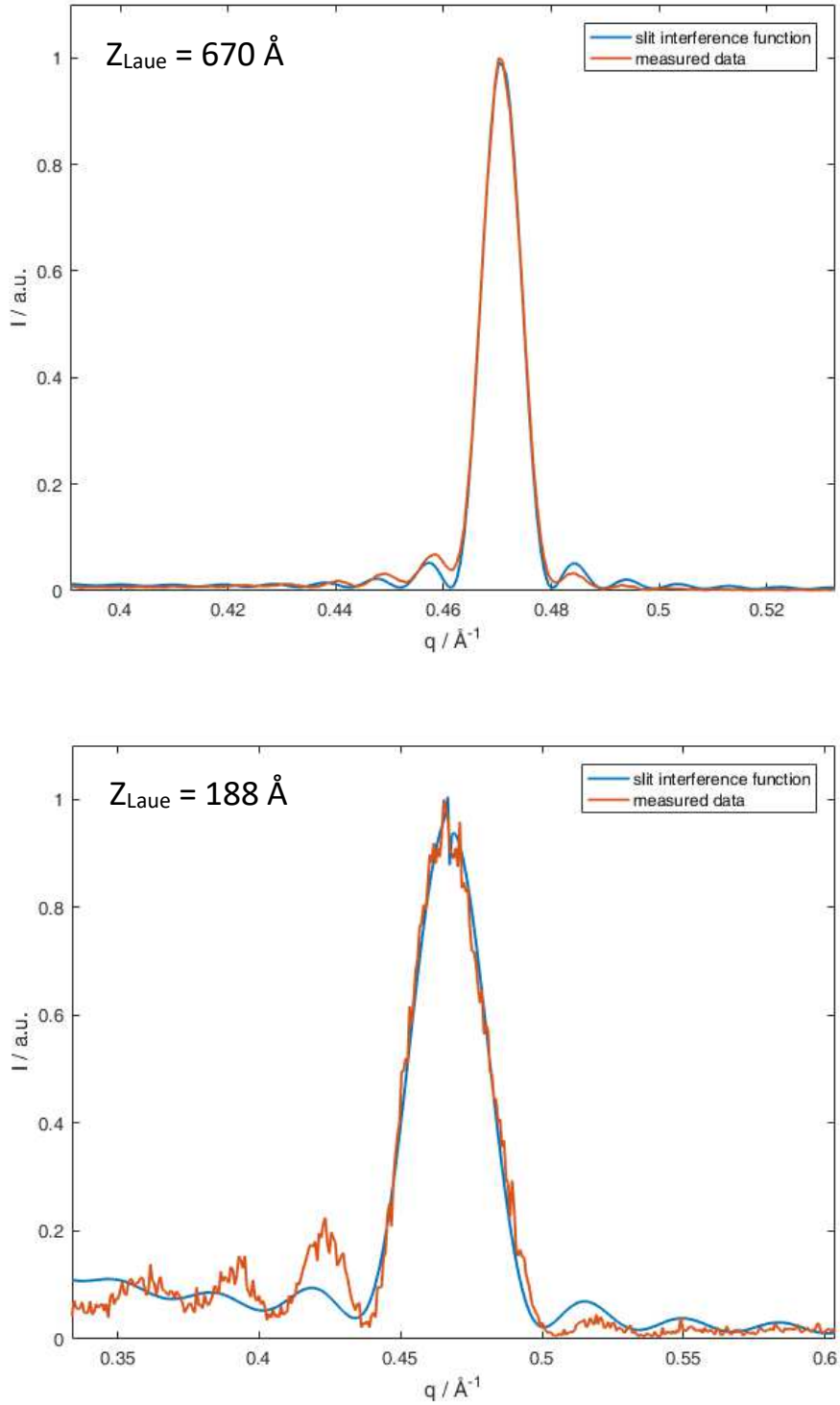

Fig. 39: Measured 002-peak of samples exhibiting the new crystal structure as well as fits obtained through the slit interference function

Comparison

A comparison of the resulting thicknesses obtained through a fit of the Kiessig fringes with the fit of the Bragg peaks through the slit interference function shows a clear difference in thicknesses.

This can be explained by the fact, that Kiessig fringes are caused by the thickness of a film with a somewhat constant electron density, which means that the entire Ph-BTBT-10 film, regardless of crystal structure is measured. In contrast, the method of fitting Bragg peaks with the slit interference function, leads to the thickness of a layer with constant crystal structure, through the broadness as well as the position of the Bragg peaks.

These methods were used on samples with varying film thicknesses, seen in Fig. 36 - 39 and the results are compared in Fig. 40. In all evaluated cases, the fit of the Kiessig fringes lead to a higher film thickness than the fit with the slit interference function. Through the origin of Kiessig fringes as well as Bragg peaks, described in the last paragraph, it can be assumed, that the already known crystal structure is still present below the new structure and only partially transforms as can be seen in Fig. 40 through the position of the intersection of the regression line with the y-axis. This regression indicates that a different structure with a thickness of approximately 21 Å is present at the interface with the substrate, as is seen in the insert in Fig. 40.

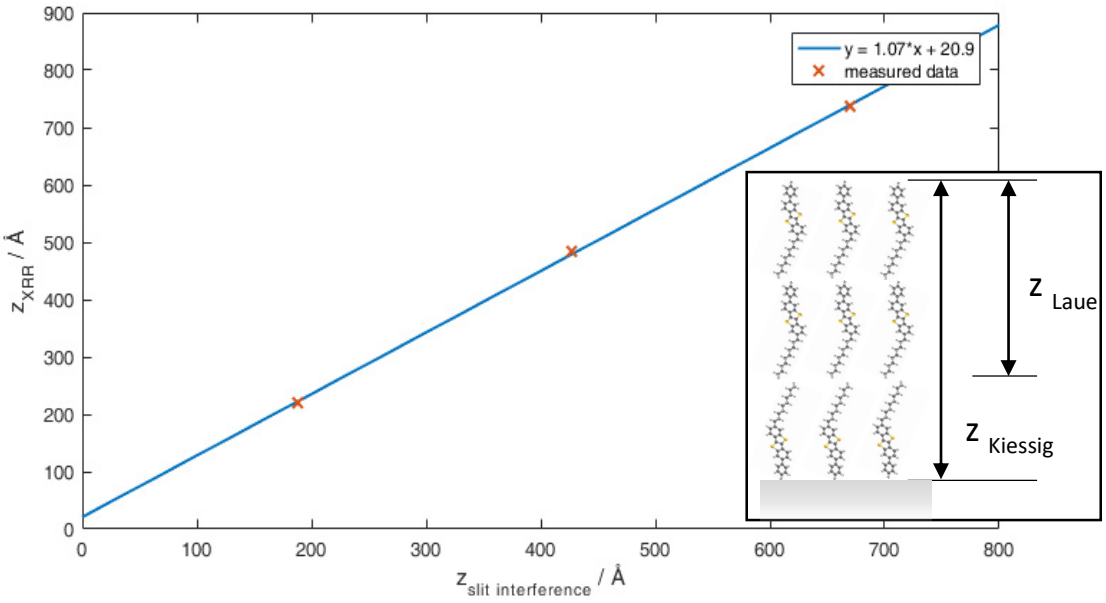

Fig. 40: Regression of thicknesses obtained through XRR-fitting as well as through the slit interference function with a model, that describes the difference in thicknesses

Specular X-Ray Diffraction

As can already be seen for lower incidence angles in Fig. 35, the measured peak positions are increasingly shifted to the left with an increase in the wavevector q. For higher angles, it becomes more apparent, that the known crystal structure doesn't fit with the measured peaks, which are more and more shifted to lower wavevectors. This becomes even clearer, when taking a closer look at the positions of the 0 0 22 – 0 0 30 peaks in Fig. 42 in comparison to the measured peaks.

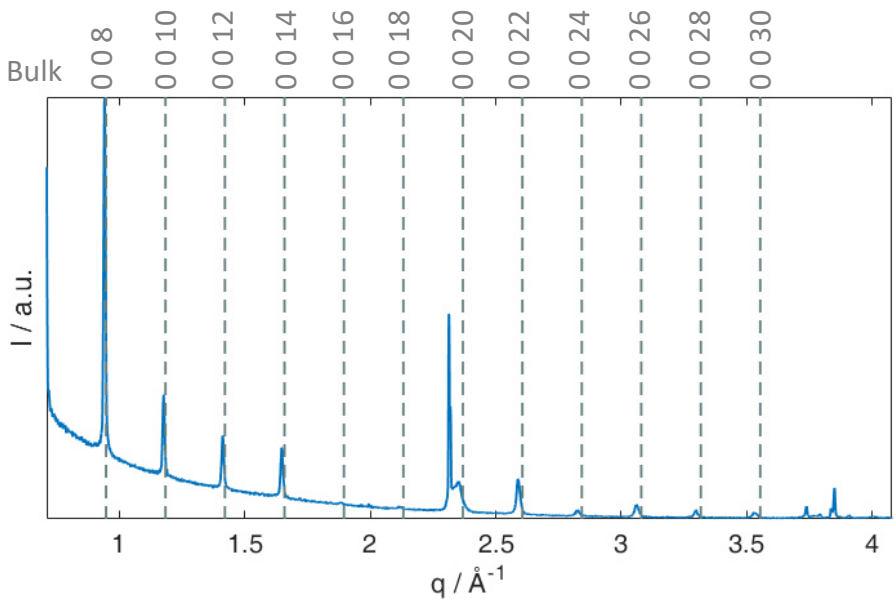

Fig. 41: Specular XRD measurement of a sample with a film thickness of 230 Å and the peak positions of the known crystal structure indicated by grey lines

Because of this, in conjunction with the fact, that a structure change is observed at a film thickness of 107 Å as well as the peak intensities not matching with the structure factor of the known phase in particular at lower angles, a new unit cell with the unit cell parameters in Table 2 is proposed.

Table 2: Unit cell parameters of the known bulk crystal structure as well as a proposed new unit cell

Unit cell parameter	Bulk	New structure
a / Å	6,05	6,00
b / Å	7,76	7,86
c / Å	53,12	26,73
α / °	90,00	90,00
β / °	93,14	93,24
γ / °	90,00	90,00
V / Å³	2489,89	1258,57
V/molecule	622,53	629,29

The proposed new structure differs from the already known one mainly in the length of the long unit cell axis, which is approximately halved compared to the bulk structure, with the d_{001} being 53,0 Å in the bulk structure and 26,7 Å in the new unit cell. This is caused by the absence of odd numbered bulk peaks for film thicknesses of more than 107 Å in X-ray reflectivity as well as specular X-ray diffraction measurements.

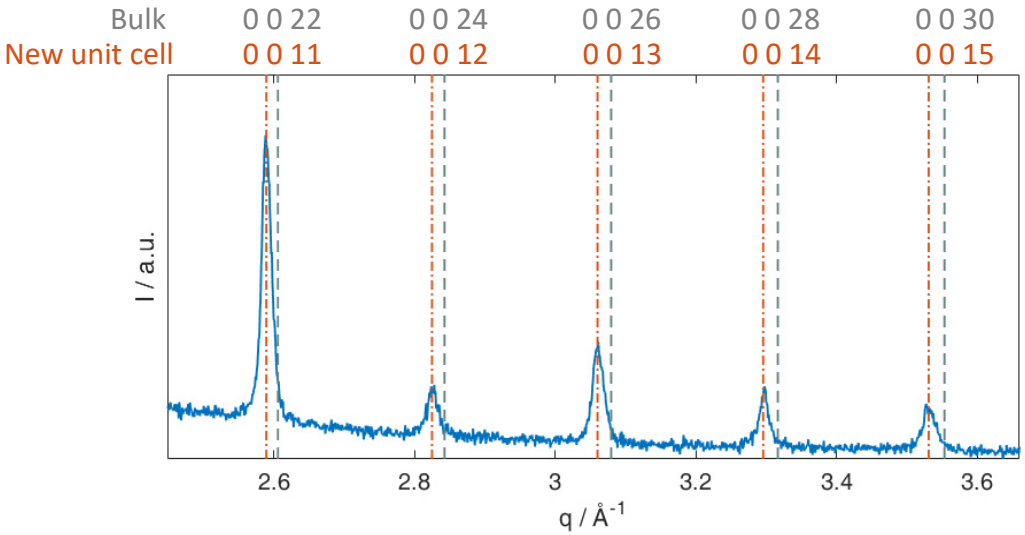

Fig. 42: Detailed image of higher order Bragg peaks with the peak positions of the even numbered peaks of the bulk phase indicated in grey and peak positions of a proposed new unit cell indicated in orange

Grazing Incidence X-Ray Diffraction

For further investigation of the crystal structure and to fully determine the unit cell size of the new structure, grazing incidence X-ray diffraction measurements were performed. The measured peak positions are slightly shifted compared to the positions of the known phase. This becomes more apparent for the 02l- as well as the 12l-rod, which are slightly shifted to lower q_{xy} values relative to the theoretical positions. In addition, further investigation of the 11l rod in Fig. 44 reveals, that the structure factor of the 112 peak of the bulk phase and the measured intensity at that position don't match. A comparison of a linescan across this rod with a sample showing the bulk structure in Fig. 44 reveals a clear difference in intensity of the 112 peak between those samples as well as differences in intensities of the 113 as well as 116 peaks.

The grazing incidence diffraction measurement further supported the evidence suggesting the presence of a new phase through a change of the positions of in-plane peaks, seen in Fig. 43 as well as a deviation in peak intensities in addition to the out-of-plane change already observed through X-ray reflectivity as well as specular X-ray diffraction measurements. Furthermore, it supports the claim, that the long unit cell axis approximately halves in length with a slight shift of the measured peak positions relative to the known bulk phase.

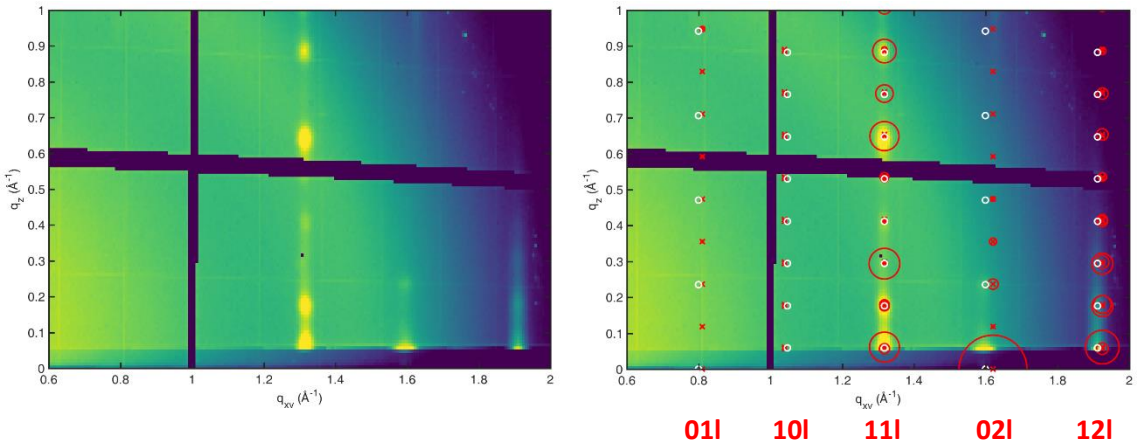

Fig. 43: Grazing incidence X-ray diffraction images of a sample with a film thickness of 230 Å measured with an incidence angle of 1° with peak positions and intensities of the bulk phase indicated in red and positions of a new unit cell indicated as white rings

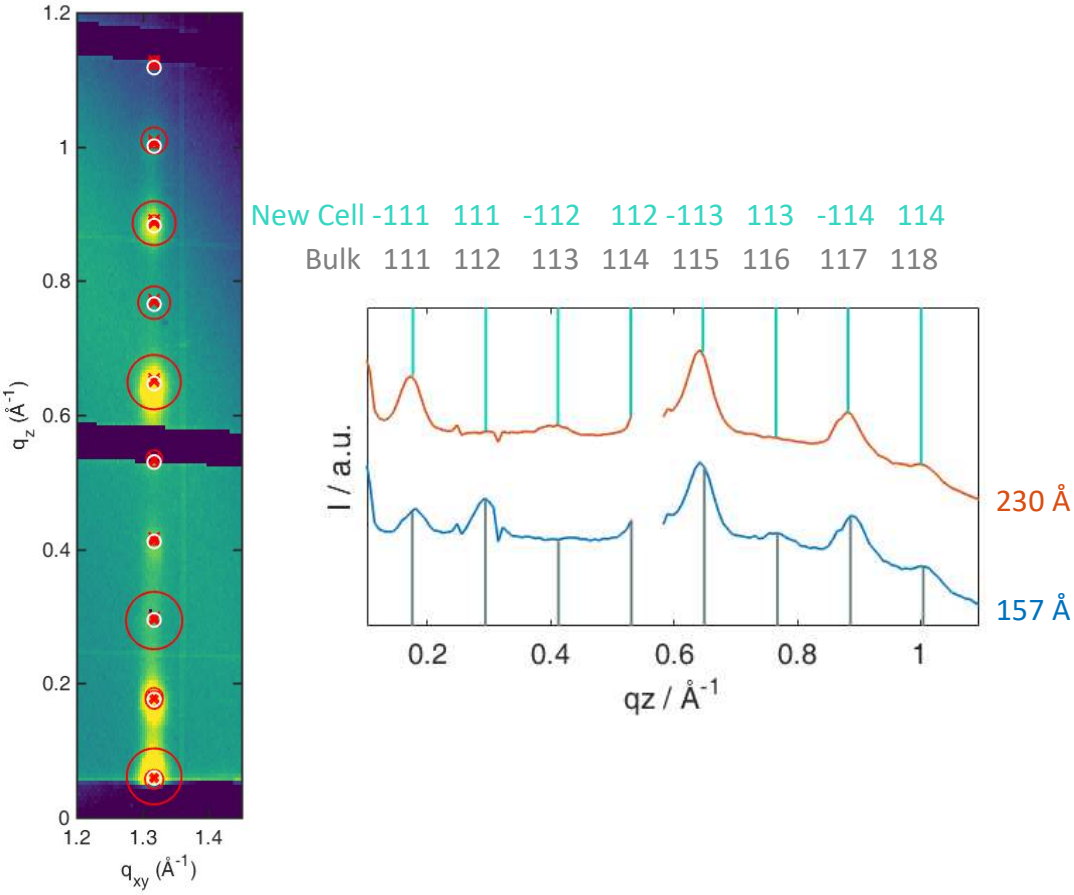

Fig. 44: Grazing incidence diffraction image of the 11l rod of a sample with a film thickness of 230 Å and an integrated line scan across this rod in comparison to a sample showing the known crystal structure and the peak positions of the bulk phase marked as well as the new crystal structure

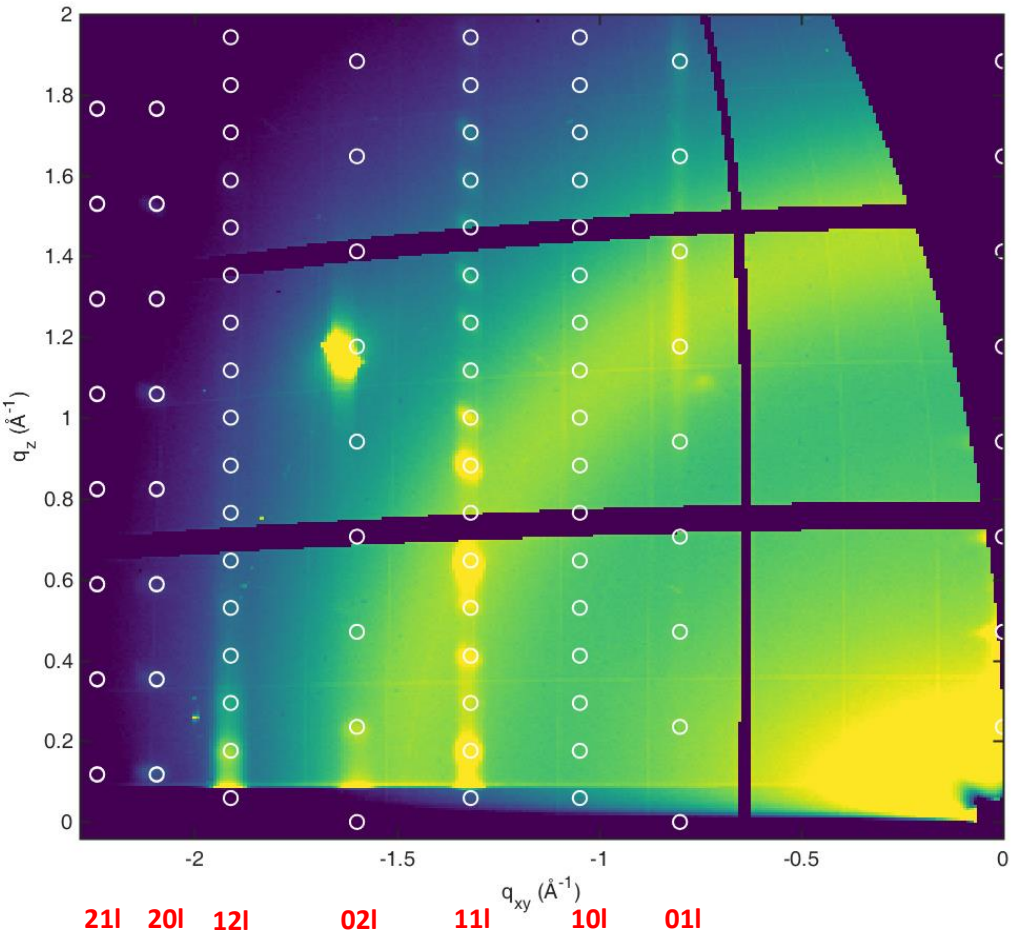

Fig. 45: Grazing incidence X-ray diffraction image of a sample with a film thickness of 484 Å measured with an incidence angle of 1° with peak positions of the new unit cell are indicated in white

Phase Transition Behaviour

In X-ray reflectivity measurements performed at increasing temperatures, a transition from the new crystal structure to the known bulk phase is observed in Fig. 46 at a temperature of 110 °C. This is indicated by a change in peak intensity of present peaks as well as the appearance of odd numbered bulk peaks. Furthermore, a transition to the *crystal E* phase can be observed at an elevated temperature.

Subsequently, the sample was further heated to 230°C, which led to a loss of the detected signal. When cooling the sample back to room temperature, the Bragg peaks didn't reappear, which can be caused by an evaporation of the film, because

the temperature of 230°C is not significantly lower than the evaporation temperature of 260 – 280 °C used during preparation of the film.

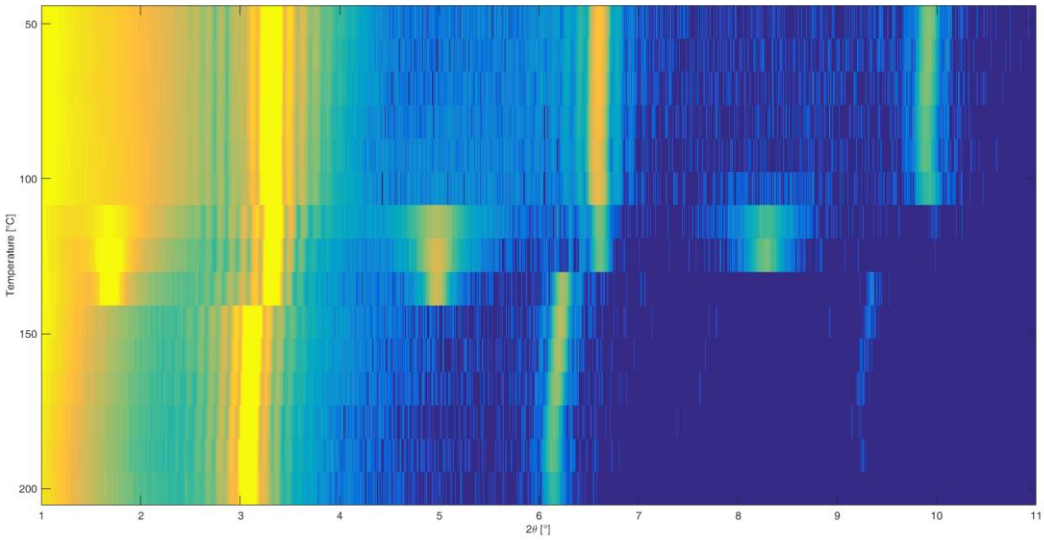

Fig. 47: X-ray reflectivity measurements with increasing temperature

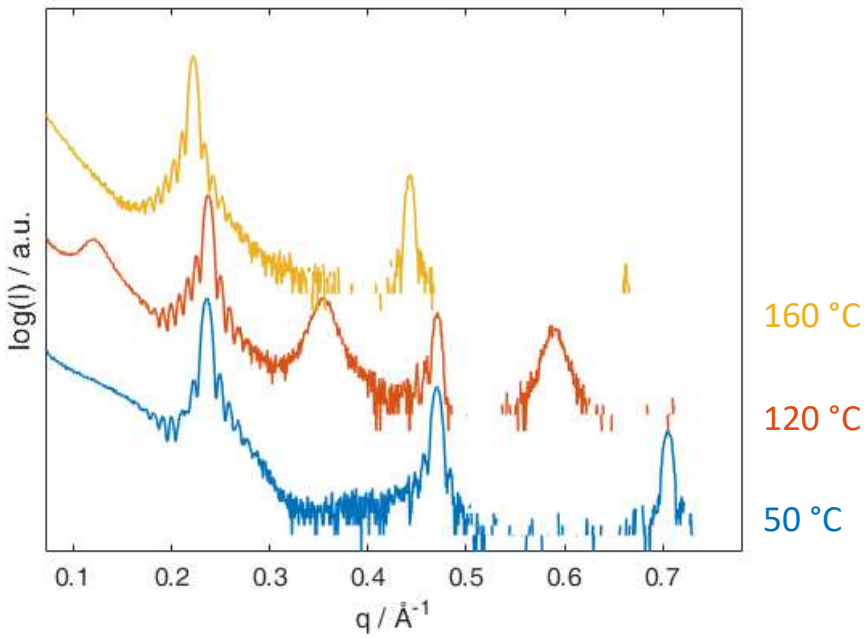

Fig. 46: X-ray reflectivity measurements at different temperatures showing the phase transitions

Conclusion

Samples with a nominal film thickness of 20 - 30 Å form molecular double-layer islands with an island height of 55 Å. Within these islands the molecules are ordered in a tail-to-tail arrangement. Film thicknesses of 50 – 81 Å exhibit the same double-layer structure with the formation of crystallites in between as well as the growth of a third layer on top of the double-layers. The known crystal structure is present in these films up to a nominal film thickness of 81 Å.

At a film thickness of 107 Å a change in morphology to lamellar islands, that become more prevalent with increasing film thickness, is observed. In addition, a change in crystal structure takes place. The new structure mainly differs from the known structure in the length of the long unit cell axis. This change is observed in specular X-ray diffraction measurements as well as X-ray reflectivity measurements through the absence of Bragg peaks at the positions of odd numbered peaks of the known structure and a slight shift of the peaks that are present relative to the bulk crystal structure. In grazing incidence diffraction measurements, the Bragg-rods of the new structure are slightly shifted in q_{xy} relative to the positions of the known structure. In addition, a change in peak intensity, especially of the 111 and 112 peak, compared to the structure factor of the known phase is measured.

Additionally, it is shown through X-ray reflectivity measurements at increasing temperatures, that the new crystal structure is a metastable phase, that converts to the known crystal structure at a temperature of about 110°C and to the crystal E structure at a temperature of 130°C for this phase transition.

Bibliography

[1] V. Coropceanu, J. Cornil, D. A. da Silva Filho, Y. Olivier, R. Silbey, and J. L. Brédas, "Charge transport in organic semiconductors," *Chem. Rev.*, vol. 107, no. 4, pp. 926–952, 2007.

[2] A. O. F. Jones *et al.*, "Substrate-induced phase of a [1]benzothieno[3,2- b]benzothiophene derivative and phase evolution by aging and solvent vapor annealing," *ACS Appl. Mater. Interfaces*, vol. 7, no. 3, pp. 1868–1873, 2015.

[3] D. Nabok, P. Puschnig, C. Ambrosch-Draxl, O. Werzer, R. Resel, and D. M. Smilgies, "Crystal and electronic structures of pentacene thin films from grazing-incidence x-ray diffraction and first-principles calculations," *Phys. Rev. B - Condens. Matter Mater. Phys.*, vol. 76, no. 23, pp. 1–6, 2007.

[4] B. Wedl *et al.*, "Crystallisation kinetics in thin films of dihexyl-terthiophene: The appearance of polymorphic phases," *RSC Adv.*, vol. 2, no. 10, pp. 4404–4414, 2012.

[5] H. L. Cheng, Y. S. Mai, W. Y. Chou, L. R. Chang, and X. W. Liang, "Thickness-dependent structural evolutions and growth models in relation to carrier transport properties in polycrystalline pentacene thin films," *Adv. Funct. Mater.*, vol. 17, no. 17, pp. 3639–3649, 2007.

[6] A. O. F. Jones, B. Chattopadhyay, Y. H. Geerts, and R. Resel, "Substrate-induced and thin-film phases: Polymorphism of organic materials on surfaces," *Adv. Funct. Mater.*, vol. 26, no. 14, pp. 2233–2255, 2016.

[7] O. Werzer *et al.*, "Interface induced crystal structures of dioctyl-terthiophene thin films," *Langmuir*, vol. 28, no. 22, pp. 8530–8536, 2012.

[8] M. Yoneya, M. Kawasaki, and M. Ando, "Are pentacene monolayer and thin-film polymorphs really substrate-induced? A molecular dynamics simulation study," *J. Phys. Chem. C*, vol. 116, no. 1, pp. 791–795, 2012.

[9] H. Chung and Y. Diao, "Polymorphism as an emerging design strategy for high performance organic electronics," *J. Mater. Chem. C*, vol. 4, no. 18, pp. 3915–3933, 2016.

[10] H. Ebata *et al.*, "Highly soluble [1]benzothieno[3,2-b]benzothiophene (BTBT) derivatives for high-performance, solution-processed organic field-effect transistors," *J. Am. Chem. Soc.*, vol. 129, no. 51, pp. 15732–15733, 2007.

[11] T. Izawa, E. Miyazaki, and K. Takimiya, "Molecular Ordering of High-Performance Soluble Molecular Semiconductors and Re-evaluation of Their

Field-Effect Transistor Characteristics," *Adv. Mater.*, vol. 20, no. 18, pp. 3388–3392, 2008.

[12] H. Iino, T. Usui, and J. I. Hanna, "Liquid crystals for organic thin-film transistors," *Nat. Commun.*, vol. 6, pp. 1–8, 2015.

[13] H. Spreitzer, "Structure and Morphology of Dioctyloxybenzothieno-benzothiophene Thin Films," Graz University of Technology, 2016.

[14] T. Hasegawa, T. Yamada, H. Minemawari, J. Tsutsumi, S. Inoue, and R. Kumai, " Crystal structure of asymmetric organic semiconductor 7-decyl-2-phenyl[1]benzothieno[3,2- b][1]benzothiophene ," *Appl. Phys. Express*, vol. 7, no. 9, p. 091601, 2014.

[15] L. G. Parratt, "Surface Studies of Solids by Total Reflection of X-Rays," *Phys. Rev.*, vol. 95, no. 2, p. 359, 1954.

[16] S. M. Danauskas, D. Li, M. Meron, B. Lin, and K. Y. C. Lee, "Stochastic fitting of specular X-ray reflectivity data using StochFit," *J. Appl. Crystallogr.*, vol. 41, no. 6, pp. 1187–1193, 2008.

[17] "https://www.elettra.trieste.it/elettra-beamlines/xrd1.html," 2019. .

[18] W. R. Bodlos, "Surface Crystallization Studies of Decyl-Phenyl-Benzothieno-Benzothiophene," Graz University of Technology, 2018.

[19] "https://www.witec.de/de/techniken/afm/," 2019. .

[20] "https://nptel.ac.in/courses/102103047/module6/lec36/2.html," 2019. .

[21] R. Resel, "Lecture Notes X-Ray Physics." 2018.

[22] R. Resel, "Lecture Notes Materials Characterisation 3." 2016.

[23] D. R. Steinmetz, "Texture evolution in processing of polystyrene- clay nanocomposites," *Thesis*, no. May, 2007.